J. Fluid Mech. (2000), *vol.* 422, *pp.* 1–54. Printed in the United Kingdom

© 2000 Cambridge University Press

Vortex organization in the outer region of the turbulent boundary layer

By R. J. ADRIAN[1], C. D. MEINHART[2] AND C. D. TOMKINS[1]

[1]Department of Theoretical and Applied Mechanics, University of Illinois, Urbana, IL 61801, USA

[2]Department of Mechanical and Environmental Engineering, University of California, Santa Barbara, CA 93106, USA

(Received 11 October 1999 and in revised form 22 May 2000)

The structure of energy-containing turbulence in the outer region of a zero-pressure-gradient boundary layer has been studied using particle image velocimetry (PIV) to measure the instantaneous velocity fields in a streamwise-wall-normal plane. Experiments performed at three Reynolds numbers in the range $930 < Re_\theta < 6845$ show that the boundary layer is densely populated by velocity fields associated with hairpin vortices. (The term 'hairpin' is here taken to represent cane, hairpin, horseshoe, or omega-shaped vortices and deformed versions thereof, recognizing these structures are variations of a common basic flow structure at different stages of evolution and with varying size, age, aspect ratio, and symmetry.) The signature pattern of the hairpin consists of a spanwise vortex core located above a region of strong second-quadrant fluctuations ($u < 0$ and $v > 0$) that occur on a locus inclined at 30–60° to the wall.

In the outer layer, hairpin vortices occur in streamwise-aligned packets that propagate with small velocity dispersion. Packets that begin in or slightly above the buffer layer are very similar to the packets created by the autogeneration mechanism (Zhou, Adrian & Balachandar 1996). Individual packets grow upwards in the streamwise direction at a mean angle of approximately 12°, and the hairpins in packets are typically spaced several hundred viscous lengthscales apart in the streamwise direction. Within the interior of the envelope the spatial coherence between the velocity fields induced by the individual vortices leads to strongly retarded streamwise momentum, explaining the zones of uniform momentum observed by Meinhart & Adrian (1995). The packets are an important type of organized structure in the wall layer in which relatively small structural units in the form of three-dimensional vortical structures are arranged coherently, i.e. with correlated spatial relationships, to form much longer structures. The formation of packets explains the occurrence of multiple VITA events in turbulent 'bursts', and the creation of Townsend's (1958) large-scale inactive motions. These packets share many features of the hairpin models proposed by Smith (1984) and co-workers for the near-wall layer, and by Bandyopadhyay (1980), but they are shown to occur in a hierarchy of scales across most of the boundary layer.

In the logarithmic layer, the coherent vortex packets that originate close to the wall frequently occur within larger, faster moving zones of uniform momentum, which may extend up to the middle of the boundary layer. These larger zones are the induced interior flow of older packets of coherent hairpin vortices that originate upstream and over-run the younger, more recently generated packets. The occurence of small hairpin packets in the environment of larger hairpin packets is a prominent feature

of the logarithmic layer. With increasing Reynolds number, the number of hairpins in a packet increases.

1. Introduction

The structure of the turbulent wall layer continues to be one of the outstanding unsolved questions in the phenomenology of turbulence. Recent promising developments concerning the near-wall portion of the inner layer, i.e. up to about $y^+ = yu^*/\nu = 50$–60 (where u^* is the wall friction velocity and ν the kinematic viscosity), focus on the role of the low-speed streaks (Jeong *et al.* 1997; Waleffe & Kim 1997). These theories and models rest upon studies of near-wall structure using experiments and low-Reynolds-number direct numerical simulations (DNS). The outer layer consists of the logarithmic layer, in which the lengthscale varies almost linearly, and the wake region in which the lengthscale approaches the boundary-layer thickness. Both layers contain eddies as small as those found in the buffer layer, as well as the much larger eddies. Much less is known about the structure of the outer layer than the buffer layer, partly because it contains a wider range of scales, making observation difficult, and partly because it is a region of larger Reynolds number, making direct numerical simulation difficult. Without a good model of the structure it is not possible to explain even the most fundamental features of the logarithmic layer. For example, why does the lengthscale grow almost linearly in the log-layer, what is the structural basis for a logarithmic (or near logarithmic) variation, and what determines empirical parameters, such von Kármán's constant or related parameters in non-logarithmic formulations? The work of Perry and co-workers, which will be discussed later, comes closest to providing such a model, but it relies on an incomplete physical description, and thus requires a number of modelling assumptions.

1.1. *Single hairpins*

The individual hairpin vortex is a simple coherent structure that explains many of the features observed in wall turbulence (Theodorsen 1952; Head & Bandyopadhyay 1981). In recent years, asymmetric hairpins or 'cane' vortices have been more commonly observed than symmetric hairpins (Guezennec, Piomelli & Kim 1987; Robinson 1991, 1993). (For brevity we shall not distinguish between symmetric and asymmetric hairpins, nor will we distinguish between hairpins and horseshoes, since available evidence suggests that these structures are variations of a common basic structure at different stages of evolution or in different surrounding flow environments. Thus, in this paper 'hairpin' will mean all hairpin-like structures, narrow or wide, symmetric or asymmetric.) Theodorsen's (1952) analysis considered perturbations of the spanwise vortex lines of the mean flow that were stretched by the shear into intensified hairpin loops. Smith (1984) extended this model and reported hydrogen bubble visualizations of hairpin loops at low Reynolds number. While there is evidence for a formation mechanism like Theodorsen's in homogeneous shear flow (Rogers & Moin 1987; Adrian & Moin 1988), it is now clear that Theodorsen's model must be modified in the strongly inhomogeneous region near a wall to include long quasi-streamwise vortices spaced about $50y^*$ apart (where $y^* = \nu/u^*$ is the viscous lengthscale), and connected to the head of the hairpin by vortex necks inclined at roughly 45° to the wall (Robinson 1991, 1993). With this simple model, the low-speed streaks are explained as the viscous, low-speed fluid that is induced to move up from the wall by the quasi-streamwise vortices. Second-quadrant ejections (positive values of the wall

normal turbulent velocity component, $v > 0$, and negative values of the streamwise velocity fluctuation, $u < 0$) are the low-speed fluid that is caused to move through the inclined loop of the hairpin by vortex induction from the legs and the head. The stagnation point flow that occurs when this ejection or 'Q2' flow encounters a fourth-quadrant (Q4) sweep ($v < 0$, $u > 0$) of higher-speed fluid moving toward the back of the hairpin is a VITA event, as defined by Blackwelder & Kaplan (1976), while the ejection and stagnation point correspond to a TPAV event as defined in the pattern recognition study of Wallace, Brodkey & Eckelmann (1977). The stagnation-point flow creates the inclined shear layer.

This scenario is substantiated by the direct experimental observations of Liu, Adrian & Hanratty (1991) who used particle image velocimetry (PIV) to examine the structure of wall turbulence in the streamwise wall-normal plane of a fully developed low-Reynolds-number channel flow. They found shear layers growing up from the wall which were inclined at angles of less than 45° from the wall. Regions containing high Reynolds stress were associated with the near-wall shear layers. Typically, these shear layers terminated in regions of rolled-up spanwise vorticity, which were interpreted to be the heads of hairpin vortices.

The flow visualizations of Nychas, Hershey & Brodkey (1973) are consistent with a hairpin vortex picture, although they were interpreted somewhat differently. Nychas *et al.* (1973) filmed solid particles in a water flow using a moving camera and identified transverse vortices in the outer layer which were formed at the top of a shear layer extending from the near-wall region to the outer region. They attributed the shear layer to low-speed fluid interacting with upstream high-speed fluid. They observed that the transverse vortices were not triggered by low-speed streaks, but they interpreted the transverse vortices to be the result of the shear layer rolling up, instead of a pre-existing hairpin. This experiment also provides a connection between the transverse vortices and the unsteady events in the near-wall layer that are associated with the widely recognized bursting process. When the transverse vortices convected downstream, an ejection sequence occurred near the wall. Finally, the motions in the near-wall region were swept away. Virtually all the Reynolds stress was produced during the sequence of events associated with transverse vortices.

Recent examination of a direct numerical simulation of a zero-pressure-gradient turbulent boundary layer at $Re_\theta = 670$ (Spalart 1988) also provides convincing evidence for the presence of hairpin loops near the wall (Chong *et al.* 1998). These loops are associated with significant Reynolds shear stress.

In the context of the hairpin model, ejections are associated with the passage of a hairpin and the attendant transverse vorticity in the hairpin head. The frequency with which ejections occur is determined by the spacing between the hairpins and their convection velocity. The frequency of turbulent bursts has been studied by many investigators using conditional averaging based upon VITA event detection schemes (Blackwelder & Kaplan 1976; Blackwelder & Haritonidis 1983; Alfredsson & Johansson 1984). In the hairpin model, each VITA event corresponds to an ejection (Q2) event caused by the hairpin. Unfortunately, there still exists controversy over the proper scaling of ejection frequency, so it is difficult to infer the proper scaling of hairpins. Often, the measured bursting frequency depends upon the values used in the VITA event detection scheme.

1.2. *Multiple hairpins in the inner layer*

Several authors, Bogard & Tiederman (1986), Luchik & Tiederman (1987), and Tardu (1995), have observed that multiple ejections in the near-wall layer commonly occur

within a single burst event. This suggests that some of the inconsistency between reported measurements of bursting frequency is associated with confusion between ejection events and bursts. In the near-wall model of Smith (1984), hairpins occur in groups of two or three along a line of low-speed fluid. These hairpins grow as they move downstream with their heads lifting away from the wall along a line inclined at 15–30° to the wall. By associating a burst with the complete group of hairpins, both the long extent of the near-wall low-speed streaks and the occurrence of multiple ejections per burst can be explained. Acarlar & Smith (1987*a*, *b*) have shown experimentally that a hemispherical bump or a steady jet of low-momentum fluid injected into a laminar boundary layer can cause periodic shedding of hairpins that looks, at first appearance, like a group of hairpins. However, the point of creation of the group is rooted at the site of the disturbance. Haidari & Smith (1994) eliminated the recurrent formation of hairpins at one site by momentarily injecting a low-momentum puff of fluid at the wall of a laminar boundary layer. They succeeded in creating one, and sometimes two hairpins, and in the case of one hairpin formed by injection they observed one additional hairpin formed by generation. Smith *et al.* (1991) have analysed the formation of hairpins extensively, and have proposed two theoretical mechanisms for the formation of multiple hairpins. An important aspect of that work is the prediction of a violent eruptive event.

In related direct numerical simulations work, Zhou *et al.* (1996, 1997, 1999) considered the evolution of an initial structure that approximated the conditional average of the flow field around a Q2 (ejection) event close to the wall in the mean turbulent flow velocity profile of a low-Reynolds-number channel flow. The initial conditional structure looked approximately like a hairpin. If its strength, relative to the background mean shear, was below a critical value the structure evolved into a single omega-shaped hairpin whose head grew until it was confined by the height of the channel (360 viscous wall units for the Reynolds number they studied). If its strength was above the critical value, the initial hairpin spawned hairpins upstream and, surprisingly, also downstream. The spawned hairpins grew and spawned further hairpins in like fashion. Except for the absence of a violent eruption, these numerical results generally support the theoretical work of Smith *et al.* (1991), and suggest strongly that multiple hairpins are formed in the low-Reynolds-number near-wall region under proper circumstances. It must be emphasized, however, that all of the evidence cited in this section is for data below $y^+ = 100$ (Smith 1984) or 200 (Zhou *et al.* 1996, 1997, 1999). Also, the single-probe data on multiple ejections were obtained mainly in the buffer layer. Hence, the results cannot be used to demonstrate the existence of hairpins or multiple hairpins anywhere except the very bottom of the outer layer.

1.3. *Hairpin structure in the outer layer*

Many of the elements of near-wall structure have been identified by hot-wire studies and conditional averaging, but direct numerical simulations at low Reynolds number (cf. Kim, Moin & Moser 1987; Spalart 1988; Brooke & Hanratty 1993, for example) were particularly important in Robinson's (1991) effort to assemble the individual observations into a more unified picture of the inner layer out to about 100–200 viscous wall units. For this reason, much of our most direct evidence about the structure of wall turbulence is confined to the low inner layer, and based on low-Reynolds-number flows that do not have a logarithmic layer. Furthermore, flow visualization, which is effective in seeing the sharp outer edge of the boundary layer, has not been as useful in the outer layer owing to the rapid diffusion of dye or smoke

in this region. Consequently, the structure of the outer layer is less well established than the near-wall region.

Despite these difficulties, it is known that the logarithmic layer contains thin shear layers, ejections, sweeps, and inclined structures (Head & Bandyopadhyay 1981; Brown & Thomas 1977; Chen & Blackwelder 1978). The range of reported inclination angles varied from 18° to 45°, suggesting these groups measured different structures, or different aspects of the same structure. If it is granted that the single hairpin vortex model offers one explanation for these phenomena, then it is reasonable to hypothesize that hairpins occur in the outer layer. Unfortunately, for the reasons cited above, it has proved very difficult to make convincing observations of hairpins in the outer region of wall turbulent flows having Reynolds numbers substantially above transition. Without such observations, it is not possible to claim that hairpins are anything more than a low-Reynolds-number phenomenon, or even a remnant of transition that is not likely to be an important part of general wall-turbulence structure.

Perhaps the strongest experimental support for the existence of hairpin vortices in the outer layer at elevated Reynolds number is given by Head & Bandyopadhyay (1981) (see also Bandyopadhyay 1980, 1983). They used a light sheet to illuminate smoke within a zero-pressure-gradient turbulent boundary layer at Reynolds numbers based on momentum thickness $500 < Re_\theta = U_\infty \theta/\nu < 17\,500$. Time-sequenced images of the boundary layer were filmed with a high-speed camera at framing rates approaching 1500 frames per second. They concluded that for Reynolds numbers up to $Re_\theta = 10\,000$, the turbulent boundary layer consists of vortex loops, horseshoes, and hairpin structures that are inclined at a characteristic angle of 45° to the wall.

Even though the spanwise dimension of the vortical structures varied significantly, Head & Bandyopadhyay (1981) proposed that, in a mean sense, their spanwise extent scaled roughly with inner variables. This scaling concept has important implications for the Reynolds-number dependency of the vortical motions. For $Re_\theta < 500$, there is no clear distinction between the large and small scales of the flow. In fact, the large-scale motions appear as single vortex loops. As the Reynolds number increases, the effect of the streamwise velocity gradient becomes more pronounced, causing vortex loops to be increasingly stretched in the streamwise direction, while becoming increasingly thinner in the spanwise direction. Consequently, characteristic low-Reynolds-number vortex loops appear like horseshoes at $Re_\theta \sim 2000$ and appear like hairpins at $Re_\theta \sim 10\,000$, according to Head & Bandyopadhyay.

Head & Bandyopadhyay (1981) also proposed that the hairpins occur in groups whose heads describe an envelope inclined at 15–20° with respect to the wall. The picture is similar to Smith's (1984) model, but instead of being based on data below $y^+ = 100$, Head & Bandyopadhyay (1981) based their construct on direct observations of ramp-like patterns on the outer edge of the boundary layer (Bandyopadhyay 1980), plus more inferential conclusions from data within the boundary layer.

Perry and colleagues have performed extensive modelling of the statistics of the turbulent wall layer in terms of a model based on randomly distributed Λ-shaped vortices (their idealization of a hairpin). Perry & Chong (1982) proposed two possible methods by which Λ-shaped vortices can grow in size with increasing distance from the wall. First, the vortices could pair to form larger vortices, creating a discrete hierarchy of Λ vortices throughout the boundary layer. Secondly, the Λ-vortices could grow continuously by drawing vorticity from the mean flow. Under certain conditions, both of these scenarios lead to a logarithmic profile for mean velocity.

Perry, Henbest & Chong (1986) extended Townsend's (1976) attached-eddy hy-

pothesis, and the near-wall model developed by Perry & Chong (1982) to encompass the entire fully turbulent region of the flow. They suggested that attached eddies with 'Kline scaling' are formed in the viscous sublayer. These eddies are stretched and either die from viscous diffusion and vorticity cancellation, or they pair and become a second hierarchy of attached eddies. This process is successively repeated, forming many hierarchies of attached eddies. It was suggested that the hierarchical lengthscales obey an inverse power-law probability distribution, which leads to a logarithmic mean-velocity profile, a constant Reynolds-stress layer, and an inverse power-law spectral region for fluctuating horizontal velocities. In addition, they proposed that the hierarchy of attached eddies is responsible for mean vorticity and most of the turbulent kinetic energy.

The objective of the present research is to gain a better understanding of coherent structures in the outer layer of wall turbulence by experimentally examining coherent structures in a zero-pressure-gradient boundary layer at Reynolds numbers $Re_\theta = 930$, 2370 and 6845. Most of the previously reported flow-visualization experiments and DNS are limited to examining details of the flow at only relatively low Reynolds numbers. In order to examine details of the turbulence at moderate Reynolds numbers, many experiments have relied primarily upon single-point measurement techniques, such as LDV or hot-wire anemometry, to obtain the required spatial resolution. In the present work, simultaneous measurements of both small-scale and large-scale motions in the streamwise–wall-normal plane are made using a high-resolution photographic PIV technique described by Meinhart (1994). The resulting vector fields provide quantitative information that makes it possible to visualize structures within boundary layers at Reynolds numbers that are higher than can be achieved using direct numerical simulations. Portions of these experiments have been presented in preliminary reports by Meinhart & Adrian (1995). The results presented here provide much more extensive direct observations of structure, which are needed to bridge the gap between structure in the low-Reynolds-number near-wall region and structure at the outer edge of the boundary layer. They definitively support a consistent picture in which packets of multiple hairpin vortices are created at the wall and grow to span the entire boundary layer, a paradigm that subsumes both the near- and far-wall evidence.

2. Experimental procedure

2.1. *Boundary-layer flow facility*

The turbulent boundary layer was developed on a horizontal flat plate placed 100 mm above the floor of the test section. To ensure spanwise uniform transition of the boundary layer and to stabilize the downstream location of the transition, a 4.7 mm diameter wire trip was placed 110 mm from the elliptically shaped leading edge of the plate, for Reynolds numbers $Re_\theta = 2370$ and 6845. For the lowest Reynolds number, $Re_\theta = 930$, the trip was moved to a location 1520 mm downstream of the leading edge allow the boundary layer to transition naturally before the trip. Reynolds numbers of the trip, based on free-stream velocity and cylinder diameter were 480, 1137 and 3264 for $Re_\theta = 930, 2370$ and 6845, respectively. In order to determine the effect of the trip upon the structure of the boundary layer, a set of PIV measurements was taken without the boundary-layer trip. The results showed no discernable differences in the boundary-layer structure.

The boundary-layer pressure gradient was directly measured by 20 static pressure

Re_θ	Re_δ	Re_λ	U_∞ ($\mathrm{m\,s^{-1}}$)	δ (mm)	θ (mm)	u^* ($\mathrm{m\,s^{-1}}$)	y^* (mm)	δ^+	H	λ/δ
930	7719	102	1.60	75.7	9.10	0.074	0.213	355	1.43	0.15
2370	20 000	189	3.79	82.8	9.84	0.158	0.099	836	1.37	0.12
6845	55 164	385	10.88	78.0	9.71	0.400	0.039	2000	1.38	0.10

TABLE 1. Boundary-layer flow parameters.

ports on the boundary-layer plate. By adjusting the contour of the test-section ceiling, the pressure gradient was made to vanish to within 0.2–3.8% of the free-stream dynamic head, depending upon Reynolds number.

Measurements were performed in an Eiffel-type low-turbulence boundary-layer wind tunnel with a working test-section 914 mm wide $\times$ 457 mm high $\times$ 6090 mm long. The root-mean square of the free-stream turbulence intensity, measured at the inlet to the test section using a 0.05 mm diameter hot-film probe, was less than 0.2%, for free-stream velocities below $10\,\mathrm{m\,s^{-1}}$. Velocity profiles, measured with hot-film anemometry at $x = 0.76, 2.28, 3.81$ and 5.33 m, showed that the boundary layer was self-similar, to within experimental uncertainty, when plotted with outer variables. The wind tunnel was designed so that the ratio between the boundary-layer thickness on each sidewall and the test-section width was less than 0.09, thereby ensuring that the boundary layer on the flat plate was two-dimensional over the central 80% of its width. The degree of two-dimensionality was determined by measuring mean velocity profiles over the entire cross-section of the wind tunnel using hot-film anemometry. The mean velocity profiles varied by less than 7% of U_∞ over the middle 80% of the test-section width.

All PIV measurements were taken 5.33 m from the leading edge. Optical access to the boundary layer was provided from the side by 305 mm $\times$ 710 mm float-glass windows, and from below by 610 mm wide $\times$ 2748 mm long float-glass windows embedded in the boundary-layer plate.

Mean velocity profiles measured with PIV agreed with hot-film anemometer measurements to within 2% of the free-stream velocity, which is within the uncertainty of the hot-film calibration. Hot-film measurements have an advantage over PIV measurements in that they usually have finer velocity resolution than PIV measurements. One advantage PIV has over hot-film anemometry is that the accuracy of the PIV calibration is independent of flow speed and thermal effects, whereas the accuracy of hot-film calibration varies significantly with flow conditions. This was particularly important at low speeds for which the uncertainty in the hot-film calibration was larger than that of PIV measurements.

2.2. *PIV measurements*

The PIV experiments were performed at three different Reynolds numbers, $Re_\theta = 930$, 2370 and 6845. The Reynolds number was changed solely by varying the free-stream velocity. Table 1 describes the boundary-layer flow conditions at $x = 5.33$ m for these Reynolds numbers. The Reynolds numbers Re_θ and Re_δ are defined using the free-stream velocity and the momentum thickness or the 99% boundary-layer thickness, respectively. The turbulent Reynolds number $Re_\lambda = \sigma_\mu \lambda / \nu$ is defined using the root-mean-square streamwise velocity, σ_μ, and the spatial Taylor microscale of streamwise velocity in the streamwise direction, λ. The Taylor microscale was

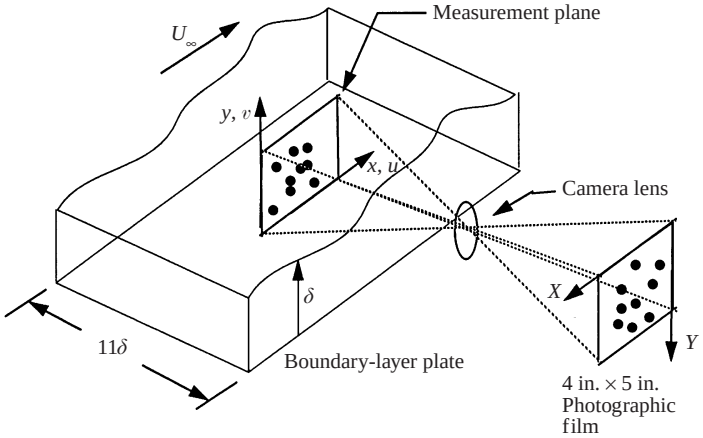

FIGURE 1. Schematic of PIV photographic recording system. The streamwise–wall-normal plane of a zero-pressure-gradient boundary layer is illuminated by a vertical laser light sheet and imaged by a side-viewing 4 in. × 5 in. photographic camera.

estimated by expanding the autocorrelation function of streamwise velocity about its origin. The viscous lengthscale is $y^* = \nu/u^*$. The von Kármán number δ^+, defined as the ratio between the boundary-layer thickness δ and the viscous lengthscale y^*, is also tabulated. It represents the range between the smallest and largest scales of motion in the flow. The shape factor H is the ratio between displacement thickness and momentum thickness.

The lowest Reynolds number, $Re_\theta = 930$, was chosen to be directly comparable to results from direct numerical simulations, cf. Spalart (1988). This boundary layer is not far beyond the transition from laminar to turbulent flow, which would occur in the range $Re_\theta \sim$300–500, depending upon the trip. The middle Reynolds number, $Re_\theta = 2370$, was chosen because a significant number of published experimental results are available at Reynolds numbers near this value. The highest Reynolds number $Re_\theta = 6845$, was above the value $Re_\theta = 6000$ at which Coles (1962) considers the wake region of the boundary layer to be roughly independent of Reynolds number. $Re_\theta = 6000$ also coincides with Re_λ exceeding 300, above which the turbulence is considered to be fully developed. Thus, we view the flow at $Re_\theta = 930$ as weak, post-transition turbulence and the flow at $Re_\theta = 6845$ as representative of moderately high-Reynolds-number boundary-layer flow. Although the behaviour at $Re_\theta = 6845$ cannot be extrapolated to very high Reynolds number without further evidence, it is certainly closer to behaving like very high Reynolds numbers than the other two flows we have studied.

The PIV measurements were performed by illuminating 0.5–2 μm diameter oil particles with a 0.25 mm thick light sheet produced by two digitally timed Nd:YAG lasers (Continuum Lasers YG660B-20). The double-pulsed images were photographed using a side-viewing 100 mm × 125 mm large-format photographic camera focused on the light sheet with a magnification of 0.826 (see figure 1). The camera lens was a 300 mm focal length $f/5.6$ Zeiss. The large-format photographic camera was used to achieve dynamic spatial range and dynamic velocity range each in excess of 100 : 1. Without a dynamic spatial range of this order, many of the results reported in this paper, which involve simultaneous observation of large and small eddies, would not be observable.

The double-exposed PIV photographs were analysed using the interrogation system described by Meinhart, Prasad & Adrian (1993) and Meinhart (1994). During interrogation, a subregion of the PIV photograph was imaged with a 1320×1035 pixel Videk Megaplus 1.4 CCD camera, and digitized with an 8-bit Imaging Technology VSI-150 frame grabber. The subregion was further divided into eight smaller subimages, and each subregion was passed to one of eight 80 MFLOP i860 array processors for analysis. Each array processor calculated twenty 128×128 pixel correlation functions per second. In practice, system overhead limited the overall interrogation speed of the eight parallel processors to about 100 velocity vectors per second. After the particle images in each subregion of the photograph were digitized, the photograph was automatically translated using a stepper motor, and a new subregion of the photograph was digitized. This process was repeated until the entire photograph was analysed, usually taking about three minutes to measure 20 000 vectors.

The local particle–image displacement was determined using the cross-correlation method described by Meinhart *et al.* (1993). The first cross-correlation window defines the spatial resolution of the velocity measurement. Its size was adjusted to be small enough to resolve the energy-containing motions, while still being large enough for strong PIV signal-to-noise (typically containing at least 10 particle–image pairs). The second cross-correlation window was chosen to be slightly larger and offset from the first cross-correlation window. The windows were chosen so that particles with first exposure images in the first cross-correlation window also had second exposure images in the second cross-correlation window. The interrogation cells were overlapped by 50% in each direction to satisfy Nyquist's sampling criterion (Meinhart *et al.* 1993).

The particle–image displacement of each interrogation cell was determined from the cross-correlation function by: (i) removing the self-correlation peak, (ii) identifying the next three largest correlation peaks as possible displacement peaks, and (iii) fitting a parabolic curve to each of the three possible displacement peaks to determine the location of each peak to within subpixel accuracy. The largest of the three possible displacement peaks was considered to be the actual displacement peak, while the other two peaks are retained as alternative displacement peaks that could be used for vector validation.

After a vector field has been calculated by interrogating a double-exposed PIV photograph, it was validated to remove erroneous velocity vectors that might have been detected incorrectly during interrogation owing to random noise in the correlation function. Both linear and nonlinear filters were used for validation. First, erroneous velocity vectors that lay outside a specified number of standard deviations from the mean velocity were tagged and removed. Typically, the tolerance was between 3.5 and 4.0 standard deviations from the mean. For this filter, the mean and root-mean-square velocities were calculated by averaging over the entire vector field, or by averaging over single rows or columns of velocity vectors in the vector field.

A median filter was used to identify erroneous velocity vectors which were not necessarily large in magnitude, but did not fit consistently with the neighbouring velocity field. The median average of each 3×3 neighbourhood was calculated and compared to the vector in the centre of the neighbourhood. If the centre vector did not agree to within a specified value of the median, it was tagged as erroneous and removed (Westerweel 1994).

After the erroneous velocity vectors were removed, the alternatively measured (second and third highest correlation peaks) velocity vectors were analysed to determine

Re_θ	Number of realizations	Number of vectors	Δx^+	Δy^+	Δz^+	$y^+_{\min}$	$y_{\min}/\delta$	$x_{\max}/\delta$	$y_{\max}/\delta$
930	60	11 700	9.0	9.0	0.9	9.0	0.025	1.5	1.2
2370	115	12 500	20	20	2.0	20.2	0.025	1.4	1.3
6845	65	26 500	36	25	5.1	38.9	0.013	1.4	1.4

TABLE 2. Resolution of the PIV experiments.

if one of them was the true velocity vector. An alternatively measured velocity vector was accepted if it lay within a specified number of standard deviations from the mean (typically 2 standard deviations), and it also fit better with the median average of the 3×3 neighbourhood than the original velocity vector.

Empty data cells occurred when erroneous velocity vectors were removed and no alternatively measured velocity vector was found. They were either filled with an interpolated velocity vector or, when there was an insufficient number of neighbouring vectors to permit reliable interpolation, they were left blank. White noise was removed from the velocity vector field by low-pass filtering the two-dimensional field with a round Gaussian kernal whose e^{-2} radius was 80% of the vector grid spacing.

The photographic technique resolved between 10 000 and 26 500 instantaneous velocity vectors in an area extending from the wall to $y/\delta = 1.2$–1.4, and covering a length of $x/\delta = 1.4$–1.5 in the streamwise direction. The small scales of motion were resolved by independent PIV measurement volumes whose physical dimensions $(\Delta x, \Delta y, \Delta z)$ corresponded approximately to $(\Delta x^+, \Delta y^+, \Delta z^+) = (9, 9, 0.9)$ at the lowest Reynolds number and $(\Delta x^+, \Delta y^+, \Delta z^+) = (36, 25, 5.1)$ at the highest Reynolds number (see table 2). The spatial resolution at either Reynolds number, but especially at the highest Reynolds number, was not adequate to resolve the smallest scales of motion near the wall. For $y^+ > 100$, the resolution in the wall-normal direction ranged from 3.2 to 5.2 Kolmogorov lengthscales. Therefore, the PIV measurements must be considered low-pass filtered estimates of the true velocity field. Fortunately, they are adequate to resolve the energy containing motions in the outer region. The interrogation spots of the PIV measurements reported here are overlapped by 50%, to minimize aliasing of the velocity signal (Adrian 1991) and to provide velocity information at every point on a 1 mm $\times$ 1 mm grid.

2.3. *PIV accuracy*

Recall that thermal anemometer velocity measurements taken in the free stream showed that the turbulence intensity of the free stream was negligibly small. The PIV measurements taken in the free stream show turbulence intensities of the order of $0.005U_\infty$. This suggests that the root-mean-square background noise of the PIV velocity measurements was less than 0.5% of the free-stream velocity.

Prasad *et al.* (1992) showed that when particle images are resolved well during digitization (i.e. the ratio of particle-image diameter d_τ to the size of a CCD pixel on the photograph, d_{pix}, is $d_\tau/d_{\text{pix}} > 3$–$4$), the uncertainty of the measurements is roughly one-tenth to one-twentieth of the particle-image diameter. The average particle-image diameter measured on the PIV photographs with a microscope was approximately $d_\tau = 50\,\mu\text{m}$. This implied that the pixel resolution for the experiments was in the range $3.13 < d_\tau/d_{\text{pix}} < 3.85$. Therefore, the particle images were adequately resolved, and the uncertainty in the measured displacement was roughly one-tenth

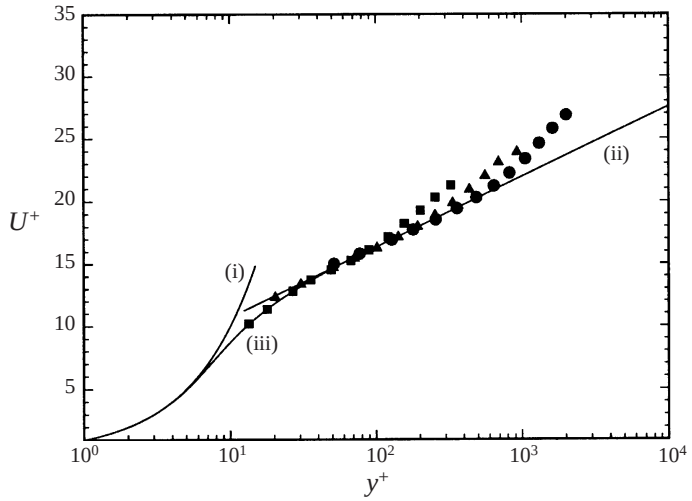

FIGURE 2. Mean streamwise velocity profiles scaled and plotted with inner variables, for ■, $Re_\theta = 930$; ▲, 2370; ●, 6845; (i) $U^+ = y^+$; (ii) $U^+ = 2.44 \ln(y^+) + 5.1$; (iii) Spalding (1961).

the diameter of the particle image, or about 5 μm. Normalizing this uncertainty with the mean displacement of the particles in the free-stream yields a relative error less than 1%.

3. Average properties of the boundary layer

The principal objective of this work is to explore the structure of the outer region using PIV to obtain quantitative images of the velocity field, a task at which photographic PIV excels. Photographic PIV data are less ideal for statistical analysis because it is tedious to obtain and analyse the large number of photographs needed for good statistical stability of the averages. The present PIV technique typically limits the number of practically obtainable photographs (i.e. independent realizations) to order 100. Since the integral lengthscale of the flow is of the same order as the measurement domain of a single photograph, each vector field was essentially one statistically independent realization. Therefore, in an ensemble of 100 photographs, the number of independent samples, of order 100, was not large enough to obtain fully converged statistics for higher-order moments, such as Reynolds shear-stress, skewness, and flatness. Even so, statistically averaged results will be presented because it is necessary to establish that the present boundary layer had properties that were typical of zero-pressure-gradient boundary layers in general, and to validate the PIV measurements to within the accuracy allowed by the statistical convergence of the averages.

Figure 2 shows the mean streamwise velocity profiles estimated by ensemble averaging the instantaneous velocity vector fields over 60–100 photographic realizations and integrating the results in the streamwise direction. The inner-variable scales were determined by estimating the friction velocity, u^*, using the chart method of Clauser (1956). (Although it is now suspected that the Clauser chart method has shortcomings, we have used it to permit consistent comparison with published data.) The mean velocity profiles show the expected logarithmic behaviour for $30y^* < y < 0.25\delta$. The mean velocity profile for $Re_\theta = 930$ agrees well with Spalding's (1961) formula

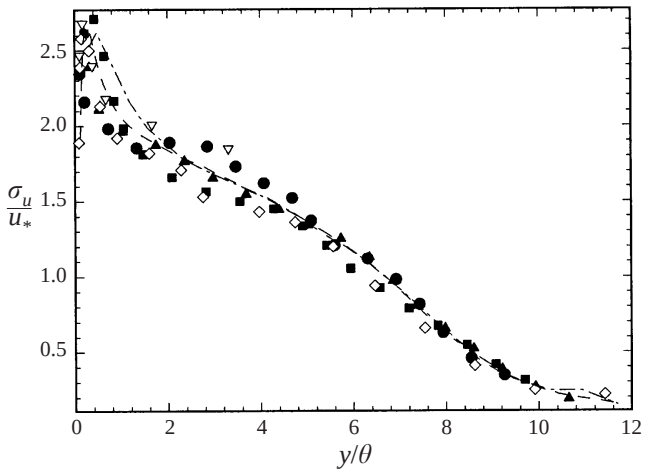

FIGURE 3. Root-mean-square streamwise velocity profiles scaled with inner variables and plotted with outer variables ■, $Re_\theta = 930$; ▲, 2370; ●, 6845; ▽, Balint *et al.* (1991); ◇, Naguib & Wark (1992); – – –, Spalart (1988) $Re_\theta = 670$; — · —, Spalart (1988) $Re_\theta = 1410$.

for the buffer region down to $y^+ = 10$, corresponding to the resolution of the PIV measurement volume.

The root-mean-square streamwise velocity is scaled with u^* and plotted in outer variables in figure 3. The momentum thickness,

$$\theta = \int_0^\infty \frac{U}{U_\infty}\left(1 - \frac{U}{U_\infty}\right) \mathrm{d}y \tag{1}$$

is chosen as the outer variable to scale wall-normal distance because it can be determined more precisely from experimental data than the boundary-layer thickness δ. The root-mean-square streamwise velocity data agree reasonably well with the results of Balint, Wallace & Vukoslavcevic (1991), Naguib & Wark (1992) and Spalart (1988), especially in the outer region for $y/\theta > 5$ (to within the differences that exist between these data). Using only the present PIV data (denoted by solid symbols), there appears to be a slight increase in root-mean-square velocity with increasing Reynolds number. According to Klewicki (1989), this Reynolds-number dependence is expected, provided that the spatial resolution of the velocity probe does not significantly attenuate the high wavenumber components of the velocity field at the higher Reynolds numbers.

In figure 4, the root-mean-square wall-normal velocity scaled with u^* is plotted against outer variables. The data agrees with the data of Balint *et al.* (1991), but they are consistently higher than Spalart's (1988) data. The differences may be due to Reynolds-number effects. The lowest Reynolds number of the present data, $Re_\theta = 930$, agrees reasonably well with Spalart's (1988) highest Reynolds number $Re_\theta = 1410$. The rest of the data, including that of Balint *et al.* (1991), are all at higher Reynolds numbers than Spalart's data, and have correspondingly higher values of root-mean-square velocity.

The Reynolds shear stress, figure 5, and the correlation coefficient, figure 6, compare well with the data of Balint *et al.* (1991) and Spalart (1988) for all Reynolds numbers.

Spanwise vorticity has been calculated at each point in the velocity field by: (i) defining a 3×3 neighbourhood centred about the point-in-question; (ii) calculating the circulation about the point-in-question by line-integrating the scalar product of the

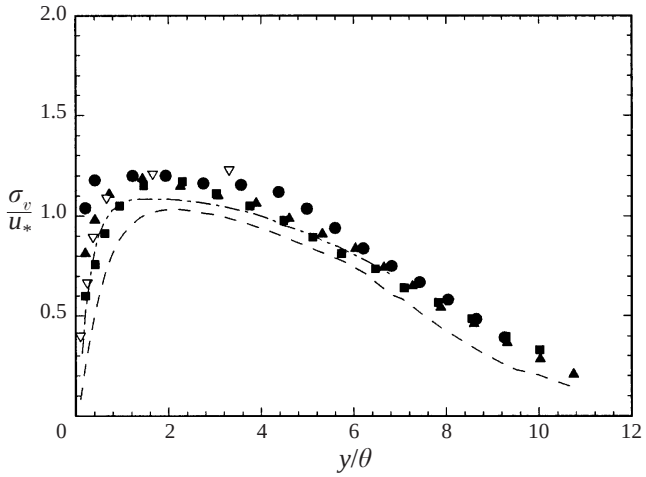

FIGURE 4. Root-mean-square wall-normal velocity profiles scaled with inner variables plotted with outer variables ■, $Re_\theta = 930$; ▲, 2370; ●, 6845; ▽, Balint *et al.* (1991); – – –, Spalart (1988) $Re_\theta = 670$; — · —, Spalart (1988) $Re_\theta = 1410$.

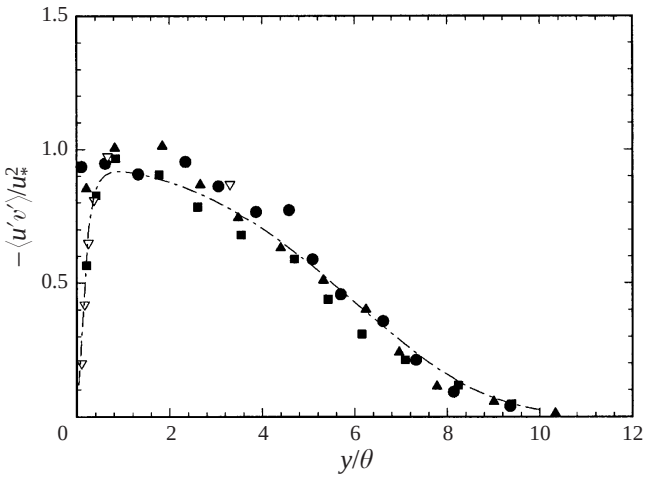

FIGURE 5. Reynolds shear-stress scaled with inner variables and plotted with outer variables for ■, $Re_\theta = 930$; ▲, 2370; ●, 6845; ▽, Balint *et al.* (1991); — · —, Spalart (1988) $Re_\theta = 1410$.

velocity vectors and the differential vector length over the eight surrounding vectors; and (iii) dividing by the area of the cell. Root mean square spanwise vorticity is then calculated by: (i) subtracting the mean vorticity from the instantaneous vorticity fields; (ii) ensemble-averaging the mean square of the fluctuating vorticity point-by-point; (iii) line-averaging the ensemble mean square vorticity field, and (iv) taking the square-root of the averaged products.

The appropriate scale with which to normalize vorticity is problematic. Klewicki & Falco (1990) determined that with adequate spatial resolution, the root-mean-square spanwise vorticity scaled with inner variables, for $1000 < Re_\theta < 5000$ for all values of y/δ; but Balint *et al.* (1991) found a contrasting result. They compared root-mean-square spanwise vorticity profiles with several other published results and found that outer variables, U_∞ and δ, collapsed vorticity profiles better than either inner variables

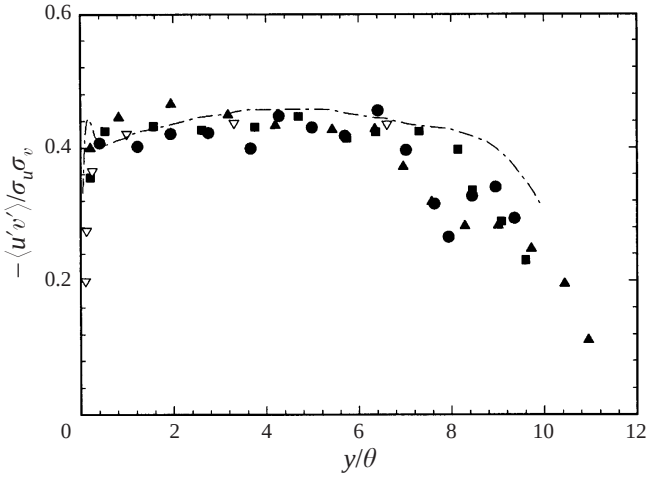

FIGURE 6. Correlation coefficient plotted with outer variables ■, $Re_\theta = 930$; ▲, 2370; ●, 6845; ▽, Balint *et al.* (1991); — · —, Spalart (1988) $Re_\theta = 1410$.

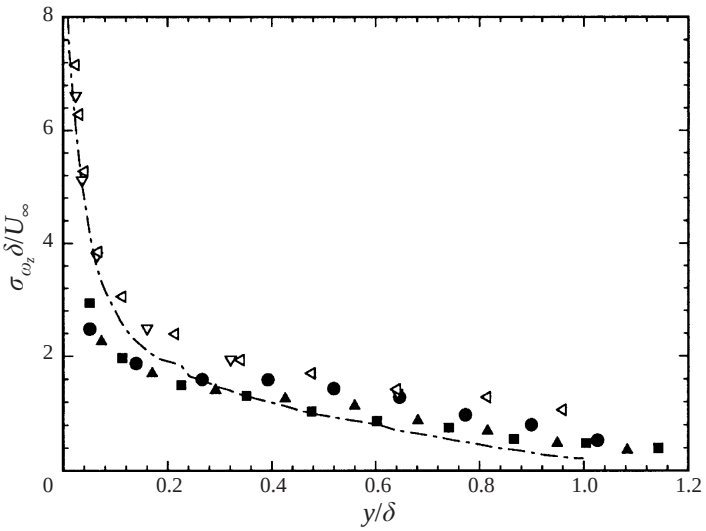

FIGURE 7. Root-mean-square spanwise vorticity scaled and plotted with outer variables ■, $Re_\theta = 930$; ▲, 2370; ●, 6845; ▽, Balint *et al.* (1991); ◁, Klewicki (1989) $Re_\theta = 2870$; — · —, Spalart (1988) $Re_\theta = 1410$.

or mixed variables. They suggested that outer variables may be appropriate because the overall mean circulation in the boundary layer is determined by the free-stream velocity and the boundary-layer thickness.

Figure 7 shows root-mean-square spanwise vorticity scaled with outer variables. For $y/\delta < 0.1$ the root-mean-square vorticity measured by PIV does not decrease as rapidly with increasing distance from the wall as the results reported by Balint *et al.* (1991), Spalart (1988), or Klewicki & Falco (1990). This is probably due to inadequate resolution of the PIV technique very near the wall. Away from the wall, for $y/\delta > 0.25$, the present PIV data lie between the data of the other investigators.

Figure 8 shows root-mean-square spanwise vorticity, ω_z, scaled and plotted with

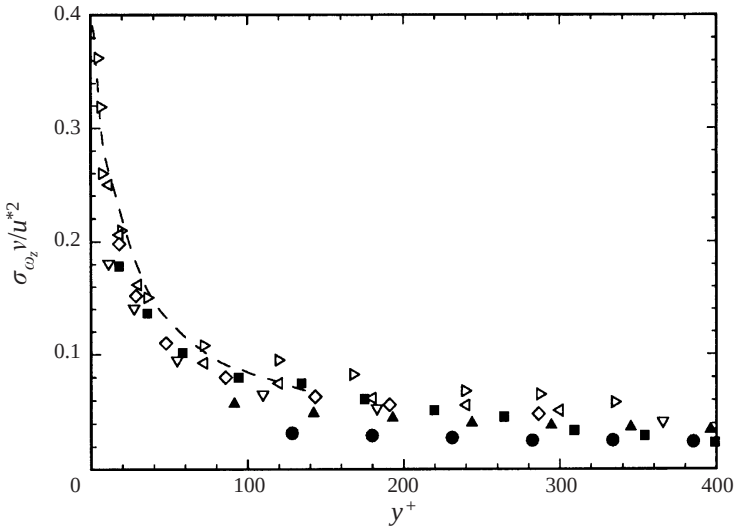

FIGURE 8. Root-mean-square spanwise vorticity scaled and plotted by inner variables ■, $Re_\theta = 930$; ▲, 2370; ●, 6845; ▽, Balint *et al.* (1991); ▷, Klewicki (1989) $Re_\theta = 1010$; ◁, Klewicki (1989) $Re_\theta = 2870$; ◇, Klewicki (1989) $Re_\theta = 4850$; – – –, Spalart (1988) $Re_\theta = 670$.

inner variables. Both the PIV results and the results of Klewicki & Falco (1990) show a decrease in root-mean-square spanwise vorticity with increasing Reynolds number, which may result from low spatial resolution, errors in measuring friction velocity, and/or spanwise vorticity not completely scaling with inner variables. In summary, above $y/\delta = 0.1$ the PIV vorticity data are consistent with the data of other experiments to within existing experimental uncertainty. Below this level, the PIV data are not spatially resolved and small-scale features of the measured flow field should only be interpreted qualitatively.

4. Visualization of the velocity vector fields

The interpretation of planar velocity vector fields is complicated by the random location of the structures in the streamwise and spanwise directions. Spanwise randomness implies that the planar data correspond to random samples of x–y cross-sections of the structures at various spanwise locations with respect to the structures. In the context of the present experiments, this difficulty can only be treated by hypothesizing three-dimensional structures that are consistent with the observed planar data and with the results of other studies. While structures inferred in this way are subject to some uncertainty, they are, nonetheless, better founded than structures inferred from one-dimensional data, as in most previous quantitative experimental studies.

4.1. *Frame of reference and identification of vortices*

A more subtle aspect of the interpretation of vector fields, two-dimensional or three-dimensional, is that the perceived flow structure depends on the way in which the velocity field is decomposed. In part, this is tied up with the problem of identifying vortical structures which has been the subject of much recent effort (Jeong & Hussain 1995; Chong, Perry & Cantwell 1990; Zhou *et al.* 1999). For the purposes of this paper it will be sufficient to follow Kline & Robinson (1989) by defining a vortex as a region of concentrated vorticity around which the pattern of streamlines is

roughly circular when viewed in a frame moving with the centre of the vortex. It has been shown (Adrian, Christensen & Liu 2000) that the foregoing method of identifying sections through vortices yields results that compare well with the vortex identification methods of Jeong & Hussain (1995), Chong *et al.* (1990) and Zhou *et al.* (1999) when applied to the vortices in wall turbulence. The combined criterion of circular streamlines in the frame moving with the vortex and concentrated vorticity leads to reliable identification by effectively eliminating regions of vorticity associated with shear and swirling regions that are non-vortical. Thus, while the methods cited above are kinematically more sophisticated, their application in this study has little if any effect on the conclusions to be drawn.

The issues of visualization will be illustrated and explained using the data in figure 9 for a single realization of the turbulent boundary layer at $Re_\theta = 6845$. Consider first the grey level plot of spanwise vorticity in figure 9(*a*). It contains many regions of concentrated vorticity. Some of the weaker fluctuations may be noise in the vorticity measurements, so we will concentrate on the strongest regions only. Some regions are elongated, but many are roughly circular, making them candidates for sections through vortices. Several (but not all) of them have been labelled A–F.

The simplest possible approach for wall flow is to decompose the field into a constant streamwise convection velocity plus the deviations therefrom. The deviation vectors are equivalent to the vectors seen in a frame of reference moving at the convection velocity. Since the Navier–Stokes equations are Galilean invariant, there is no dynamical basis for preferring one frame over another, and we are at liberty to use the convective frame that provides the best visualization of the vector field. In figures 9(*b*) and 9(*c*) the velocity vector field corresponding to figure 9(*a*) is shown after subtracting, respectively, convection velocities $U_c = 1.0U_\infty$ and $U_c = 0.8U_\infty$. In figure 9(*b*) the vectors generally have negative streamwise components relative to the free-stream velocity, as expected. At the instantaneous edge of the boundary layer in figure 9(*b*), it is possible to observe a pattern of nearly circular streamlines that coincides with the vorticity concentration labelled A in figure 9(*a*). Following the criteria adopted above, we interpret this to be a cross-section through a concentrated vortex. The regions labelled B and C also contain concentrated vorticity, but their velocity pattern is barely circular in figure 9(*b*) because their convection velocities differ from U_∞ by about 10%. If the convection velocity is changed appropriately, the velocity vector pattern of B or C does look circular and the centre coincides with the maximum vorticity. Unlike regions A–C, the regions of concentrated vorticity labelled D, E and F are not even remotely circular vortices in the frame of reference used in figure 9(*b*).

Now consider figure 9(*c*). It is the same vector field as figure 9(*b*), except $U_c = 0.8U_\infty$. In this frame of reference, the vortex structures A, B, and C can no longer be identified with circular streamlines, nor can the other regions of concentrated vorticity D, E and F. Instead, a series of near-wall shear layers, visible as dark bands inclined at 30–50° to the wall, can be observed below $y/\delta = 0.1$ in the region where vorticity concentrations D–F reside. They are associated with Q2 events. The same pattern exists in figure 9(*b*), but it is much less apparent owing to the large negative velocity of the near-wall vectors in that frame. The inset to figure 9(*c*) shows a magnified view of the vector field associated with the three vorticity maxima D, E and F using a convection velocity of $U_c = 0.6U_\infty$. When depicted in this manner it is clear that the inclined shear layers are associated with the compact, circular vortex patterns labelled D, E and F in the inset. Since each of these vortex patterns has zero velocity at its centre, their streamwise speed of translation must be approximately $U_c = 0.6U_\infty$.

The foregoing example shows that the vector field pattern associated with an approximately circular concentration of vorticity, i.e. a vortex core, appears to be a circular streamline pattern if and only if the convection velocity matches the velocity at the centre of the vortex. That is, the convection velocity must be equal to the velocity with which the vortex pattern is translating in order for the velocity pattern to look like a vortex.

Various investigators have reported discrepancies between the locations of vorticity maxima and the apparent centres of rotation of the velocity vector patterns, from which they concluded that a compact local maximum of the vorticity is not a reliable indicator of the presence of a vortex. However, our experience has been that when viewed in a convecting frame that makes the vector pattern look most like that of a compact circular vortex, the location of the local maximum of the vorticity coincides closely with the zero vector of the vector pattern. Thus, by systematically changing the convection velocity in small increments such as $0.05U_\infty$ while viewing each PIV vector field and its associated vorticity field on a high-resolution computer monitor, all of the compact vortices in figure 9(*a*) can be identified.

Reynolds decomposition by subtracting the long-time-averaged velocity field from the instantaneous velocity field is the traditional technique for decomposing turbulent velocity fields. It has been used almost universally for analysis of turbulent signals, and it is a natural approach from a mathematical viewpoint. We find, however, that when interpreting the structure of instantaneous velocity vector fields, Reynolds decomposition often distorts the instantaneous structure, and in certain situations, may actually mislead the analysis (Adrian *et al.* 2000). Figure 9(*d*) shows the Reynolds decomposition of the velocity field. While certain features in figures 9(*b*) and 9(*c*) can also be observed in figure 9(*d*), many of the structural elements are distorted, especially in the vertical direction near the wall where the mean velocity profile has a high rate of curvature. For example, the inclined shear layers that occur in the range $0.05 > y/\delta > 0.1$ in figure 9(*c*) are less evident in the Reynolds-decomposed vector field. If the vortices travel with the long-time-averaged mean velocity, the mean velocity would be the same as the local convection velocity, and the fluctuating field obtained by Reynolds decomposition would reveal the vortices clearly. This procedure should work when the turbulent flow can be adequately described by a mean plus small random fluctuations. However, in the case of boundary-layer flows, the turbulence intensity is relatively large near the wall. We have examined several hundred realizations in the streamwise wall-normal plane, and we have found very few realizations in which the profiles of the streamwise velocity even vaguely resemble the long-time-average mean velocity profile. As a consequence, the Reynolds decomposed fluctuating field is less readily interpreted.

The principles illustrated by the single realization in figure 9 are supported by experience with thousands of vector fields in this and other PIV studies. Examining velocity vector fields with many different Galilean frames of reference provides a more physical representation of the turbulent flow field than examining vector fields using Reynolds decomposition. Therefore, in studying the experimental vector fields and in arriving at the conclusions to be presented, we have examined each instantaneous realization by subtracting up to 20 different constant convection velocities before drawing conclusions about the instantaneous structure of the flow field. The simplest rule we have found is that *at a given convection velocity, the patterns of those vortex cores that are moving with velocity equal to the selected convection velocity can be seen.* With changing convection velocity, the vortices in different regions of the flow become more or less apparent.

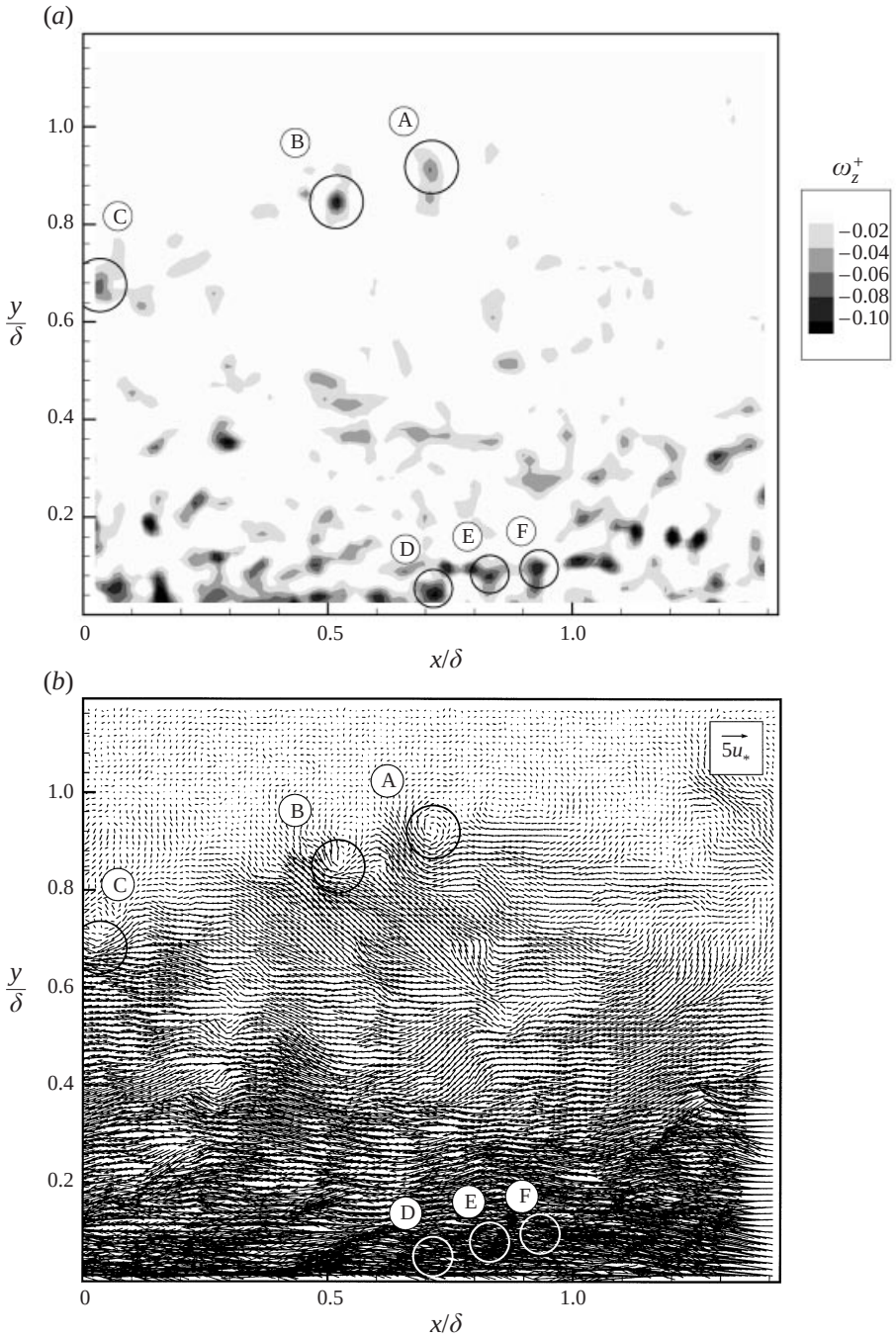

FIGURE 9(*a*, *b*). For caption see facing page.

Vector fields viewed in different Galilean frames have additional properties that are useful for interpretation. First, velocity vectors having streamwise components nearly equal to the convection velocity are small in magnitude, and regions containing such vectors generally appear light to the eye. In contrast, regions in which the

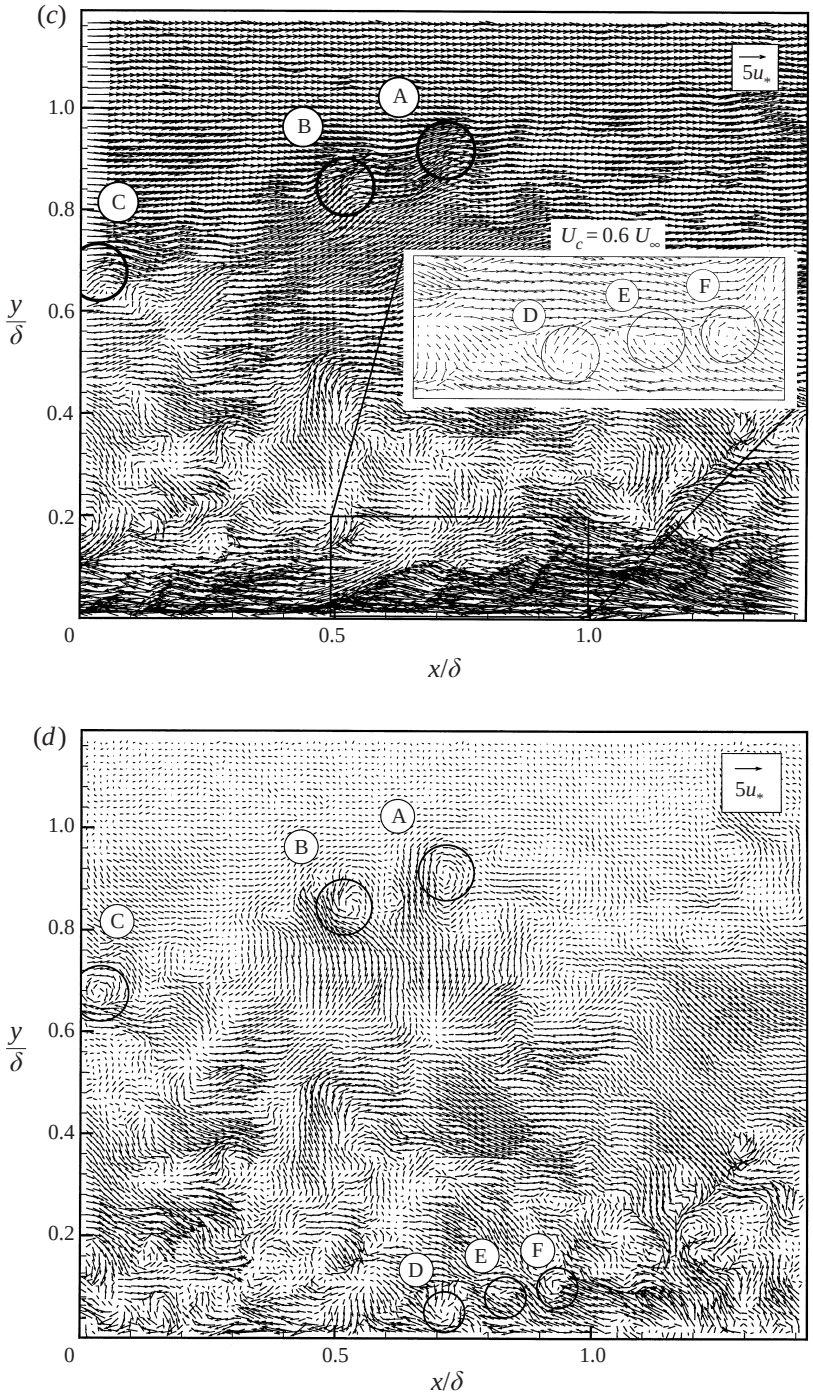

FIGURE 9. Streamwise wall-normal velocity vector field at $Re_\theta = 6845$ shown using several different types of vector decomposition: (*a*) spanwise vorticity; (*b*) vectors viewed in a frame of reference convecting at $U_c = 1.0U_\infty$; (*c*) vectors viewed in a frame-of-reference convecting at $U_c = 0.8U_\infty$; (*d*) Reynolds decomposed fluctuating vectors.

streamwise velocity differs greatly from the convection velocity appear dark because they consist of long positive or negative velocity vectors. One advantage of Galilean decomposition, as opposed to Reynolds decomposition, is that relative shears between adjacent structures in the flow are preserved. Secondly, the invariance of the Navier–Stokes equations under Galilean transformation means that the fluctuations about the convection velocity can be interpreted directly in terms of the Navier–Stokes equations without modification for the mean Reynolds stress.

4.2. *Hairpin vortex signatures*

The flow pattern associated with the vortex labelled A in figure 9(*a*) and the vortices in the inset to figure 9(*c*) possess important additional characteristics. Below and upstream of the circular streamlines in each pattern there is a region of strong second-quadrant vectors ($u - U_c < 0$ and $v > 0$) which occurs on a locus that is inclined at roughly 45° to the x-direction. The spatial extent of the region of Q2 vectors is approximately the same as the diameter of the region of circular streamlines, and the velocity vectors in the Q2 region are directed at approximately 135° to the x-direction. Note these ejections are also visible in the Reynolds decomposed field (figure 9*d*), as their associated vortices happen to be convecting at a speed close to the long-time average.

Figure 10(*a*) schematically depicts the qualitative signature of the velocity field induced by an idealized (not necessarily symmetric) hairpin vortex on a streamwise–wall-normal plane that cuts through the centre of the hairpin. It is assumed that the hairpin is attached to the wall. Following Robinson (1991, 1993) the various parts of the hairpin are called the head, neck and legs, the latter being prominent in the wall buffer layer. The velocity pattern in an x–y cross-section of the hairpin contains the following features: (i) a transverse (i.e. spanwise) vortex core of the head rotating in the same direction as the mean circulation; (ii) a region of low-momentum fluid located below and upstream of the vortex head, which is the induced flow associated with the vorticity in the head and neck; (iii) an inclination of this region at approximately 35–50° to the x-direction below the transverse vortex and more nearly tangent to the wall as the wall is approached. In the buffer layer, the legs of the hairpin become quasi-streamwise vortices that induce low momentum fluid upwards. Similar behaviour has been found in direct numerical simulations (Adrian, Moin & Moser 1987; Kim 1987), wherein the quasi-streamwise vortices cause fluid from the viscous boundary layer at the wall to lift away from the wall and form the near-wall low-speed streaks that are commonly observed in the buffer layer (Robinson 1993). Frequently, a fourth-quadrant Q4 event ($u - U \geqslant 0$, $v \leqslant 0$) is observed to oppose the Q2 event, forming a stagnation point and an inclined shear layer upstream. A Q4 event observed in a frame convecting with the eddy can be explained if the hairpin either lies in the downwash of an upstream eddy, or if it propagates more slowly than the surrounding fluid.

A pattern containing the elements described above (circular streamlines, a strong Q2 event in a region having approximately 45° inclination, and a Q4 event with a stagnation point) is consistent with the vector pattern that would be seen if the laser light sheet of the PIV cut through the mid-plane of a hairpin vortex. It is idealized in figure 10(*b*). These two-dimensional patterns have been clearly associated with three-dimensional hairpins in homogeneous shear flow (Adrian & Moin 1988) and in conditionally averaged three-dimensional fields of wall turbulence when conditioned on the occurrence of a Q2 event, i.e. a second-quadrant vector (Adrian *et al.* 1987; Adrian 1996; Zhou *et al.* 1999). For this reason, we shall refer to a velocity vector

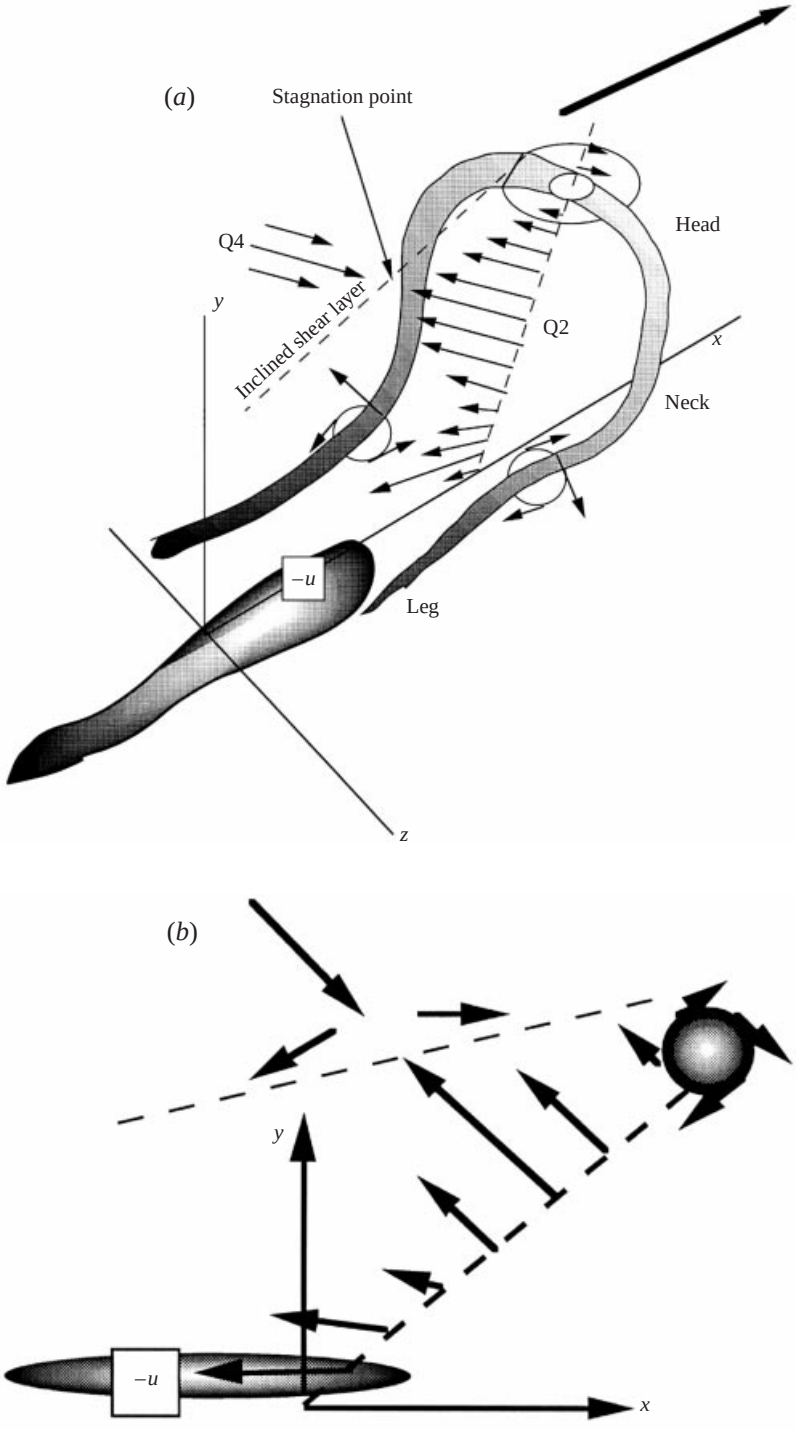

FIGURE 10. (*a*) Schematic of a hairpin vortex attached to the wall and the induced motion. (*b*) Signature of the hairpin vortex in the streamwise–wall-normal plane. The signature is insensitive to the spanwise location of the plane, until it intersects the concentrated core forming either side of the hairpin.

pattern having a circular vortex with an inclined region of Q2/Q4 vectors beneath it (figure 10*b*) as a hairpin vortex signature, or HVS. A hairpin would not need to be symmetric in order to induce this pattern of motion, so the HVS can also be the signature of an asymmetric hairpin (or 'cane' vortex in the terminology of Robinson 1991, 1993). A second HVS can be seen at the edge of the boundary layer near $x/\delta = 0.5$ in figure 9.

The hairpin vortex signature is fully consistent with the existing body of results on the structure of wall turbulence. In particular, the transition from a Q2 to a Q4 event is consistent with the VITA event that is normally used to identify a turbulent bursting process (Robinson 1991). The stagnation point on the inclined shear layer upstream of each hairpin is the centre of a transition from the Q2 event under the head of the hairpin to an upstream Q4 event. As shown by Wallace *et al.* (1977), this is the site normally identified by the VITA analysis of Blackwelder & Kaplan (1976). Imagine the hairpin passing over a fixed single-point probe located at approximately the height of the stagnation point. Initially, the u- and v-velocities are weak. As the hairpin approaches the probe, the streamwise velocity would become increasingly negative and the v-component would become positive owing to the upward induced flow under the head of the hairpin. When the stagnation point on the shear layer behind the hairpin reaches the probe, both components would vanish and change signs immediately thereafter. Upstream of the shear layer the u- and v-components would become increasingly positive and negative, respectively, then decay as the hairpin moved further downstream of the probe. This description also coincides closely with the pattern recognition (TPAV) results of Wallace *et al.* (1977).

The present (x, y)-plane data are ill-suited to revealing quasi-streamwise vortices, but the computations of Zhou *et al.* (1996, 1997, 1999) and the work of Smith (1984) and Smith *et al.* (1991) clearly indicate that when viewed properly, the hairpin vortices that appear close to the wall have long legs that are the quasi-steamwise wall vortices associated with the low-speed streaks in the buffer layer. Hairpin vortices that occur far from the wall, such as those labelled A–C in figure 9(*a*) may not possess quasi-streamwise vortex legs, being instead more similar to those seen in homogeneous turbulent shear flow (Adrian & Moin 1988).

5. Structure in the outer region

5.1. *Frequency of hairpin vortex signatures*

We find that there are many hairpin vortex signatures in each of the vector fields measured at each Reynolds number. In fact, the hairpin vortex signature is the single most readily observed flow pattern in the (x, y)-plane data. The reader can confirm this by looking ahead to the vector fields that will be presented for the various Reynolds numbers, bearing in mind that the depiction of a vector field for any one value of the convection velocity does not clearly show all of the hairpin vortex signatures. This point is demonstrated clearly by figure 9(*a*) in which there are many regions of concentrated vorticity, almost all of which correspond to a hairpin vortex signature when viewed in the proper frame of reference.

The discussion of structure will be restricted to the outer region, $y^+ > 30$, where the PIV measurements have been shown to be reliable. This region excludes much of the quasi-streamwise vortex portion of a near-wall hairpin. All PIV fields will be shown in a frame having fixed physical dimensions, corresponding to outer scaling.

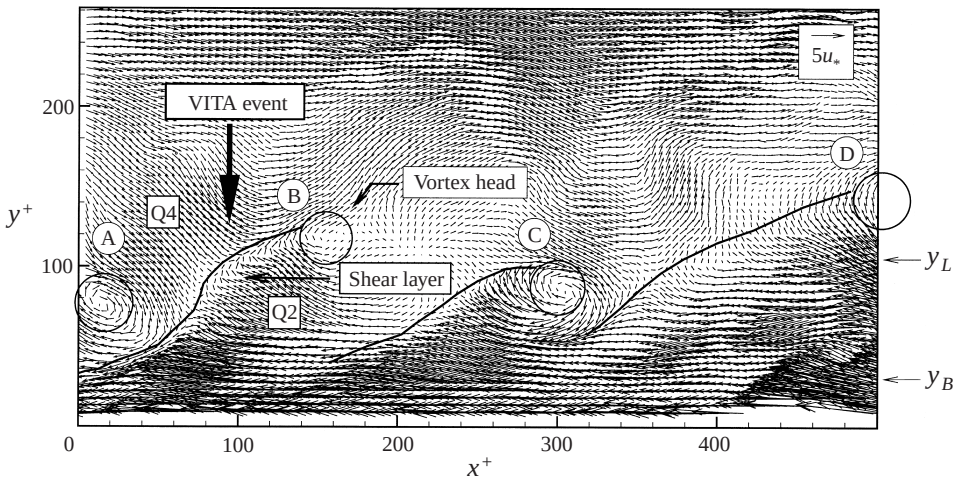

FIGURE 11. Near-wall realization at $Re_\theta = 930$ showing four hairpin vortex signatures aligned in the streamwise direction. Instantaneous velocity vectors are viewed in a frame-of-reference moving at $U_c = 0.8U_\infty$ and scaled with inner variables. Vortex heads and inclined shear layers are indicated schematically, along with the elements triggering a VITA event.

5.2. *Hairpin vortex packets*

A primary conclusion drawn from the present experimental observations is that hairpin vortex signatures very frequently occur in groups, and that the individuals within these groups propagate at nearly the same streamwise velocity, so that they form a travelling packet of hairpin vortices. Figure 11 provides a clear example of this behaviour from the $Re_\theta = 930$ boundary layer. The velocity-vector map is viewed in a convective frame of reference $U_c = 0.8U_\infty$. Four vortices, denoted A–D, are located in the range $80 < y^+ < 140$, with streamwise spacing of 120–160 viscous wall units. (In this and future diagrams, the nominal tops of the logarithmic layer and buffer layer are indicated by $y_L = 0.25\delta$ and $y_B = 30y^*$, respectively.) Spanwise vortices B,C and D each possess the characteristics of a hairpin vortex signature. The fact that all of the vortex heads are nearly circular means that they are being viewed in a frame that is moving with the convection velocity of the heads. Put another way, each of the heads circled in figure 11 is moving at approximately $U_c = 0.8U_\infty$, i.e. the four hairpins are moving together as a packet. The essential elements of the packet pattern are indicated schematically, as well as the elements comprising a VITA event. The inclined shear layers associated with the vortices are identified visually as the locus of points across which the vector direction changes abruptly. They are indicated by solid lines.

Examination of several hundred instantaneous velocity-vector fields reveals, for each of the Reynolds numbers studied, that it is common to see multiple hairpin vortex signatures in close spatial proximity to each other in the streamwise direction and convecting with nearly the same velocity. (Histograms of the convection velocity indicate that the velocity dispersion is less than 10% of the free-stream velocity.) In fact, we find at least one hairpin vortex packet in 85% of all PIV images. Next to the hairpin vortex signatures, the hairpin vortex packets are the most commonly observed structure in our wall turbulence data, and like the individual vortices they have some variation in group convection velocity from packet-to-packet at a given y-location.

The patterns that are identified as the signatures of hairpin packets in near-wall

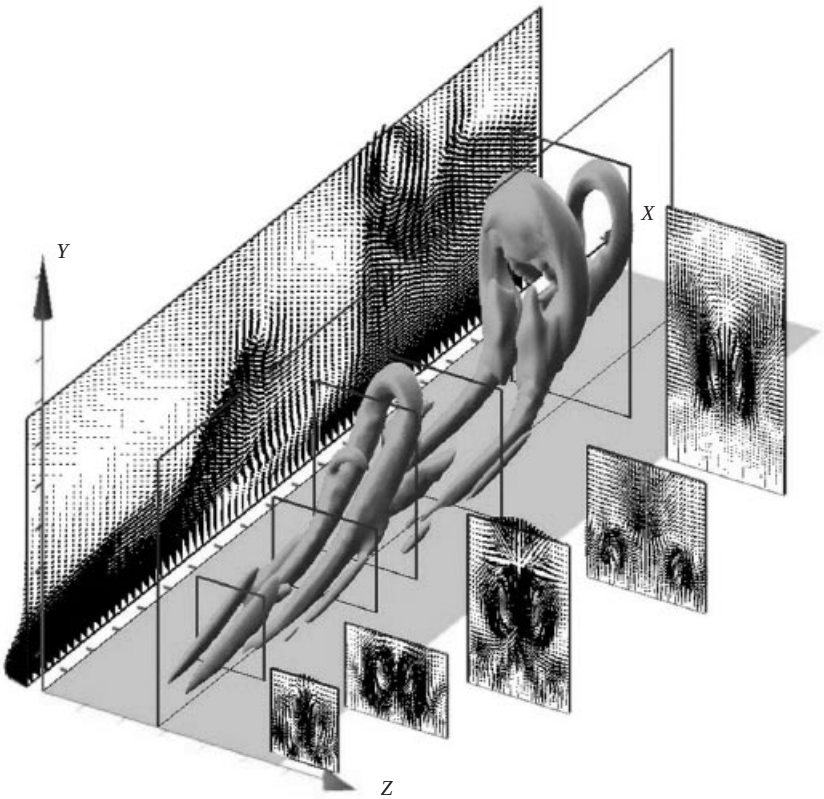

FIGURE 12. Hairpin vortices computed by Zhou *et al.* (1999). The velocity vector field in the plane lying midway between the legs is qualitatively similar to the hairpin vortex signature shown in figures 10(*b*) and 11.

boundary-layer turbulence compare very well with the x, y patterns associated with the hairpin packet computed for channel flow by Zhou *et al.* (1999). Figure 12 shows a computational result for the packet that evolves out of a single hairpin-like initial disturbance. The largest hairpin in the packet is the primary hairpin that gave birth to the packet. It has spawned complete secondary hairpins both upstream and downstream, and the upstream hairpin is in the process of spawning tertiary hairpins, one close to the wall, and one closer to the neck of the secondary. The flow pattern in the (x, y)-plane passing through the middle of the packet possesses all of the same characteristics as the patterns observed in the experimental boundary layer: vortex heads, inclined regions of Q2 vectors, stagnation points, and inclined shear layers upstream of each hairpin. This point-by-point similarity provides a strong basis for associating the two-dimensional patterns observed in our experiments with three-dimensional packets of the general form of the one shown in figure 12.

Streamwise histories of streamwise velocity, wall-normal velocity, and Reynolds stress of the field in figure 11 at $y^+ = 30, 50$ and 100 are given in figure 13. The characteristic features of the hairpin vortex signatures in figure 11 create clear imprints in the streamwise variation. For example, at $y^+ = 50$ the streamwise velocity profile exhibits three peaks of low momentum (at $x^+ = 100, 290$ and 420), each of which corresponds to fluid directly underneath the heads of hairpins B, C and D. This fluid has low momentum because it is being ejected away from the wall by the hairpins,

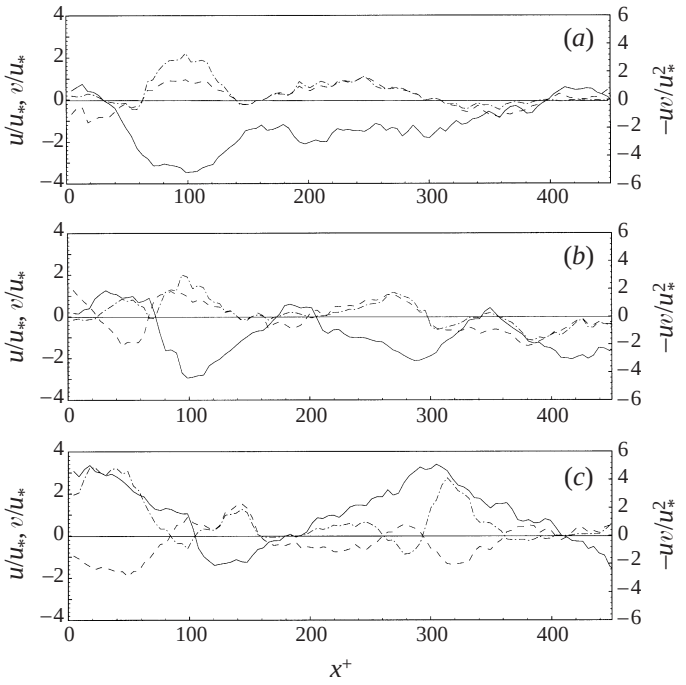

FIGURE 13. Traces of the instantaneous ——, u'; – – –, v'; and —·—, $u'v'$ through the vector field in figure 11 show that the form of the VITA event is associated with the signature of a hairpin vortex; (*a*) $y^+ = 30$; (*b*) $y^+ = 50$; (*c*) $y^+ = 100$. $Re_\theta = 930$.

i.e. the v-component is positive. The regions along the x-axis at which the u- and v-components change signs correspond to the stagnation points on the shear layers. The maximum values of the instantaneous product $-uv$ occur fore and aft of the stagnation points, making these regions critically important to the creation of mean Reynolds shear stress. Note that as the wall is approached, the quasi-streamwise legs begin to contribute long regions of Q2 events by pumping very low-momentum fluid up from the viscous layer, cf. figure 13(*a*).

As noted above, the profiles of streamwise and vertical velocity created by a single hairpin resemble the pattern-recognized velocity profiles found using time histories measured by hot-wire anemometry (Wallace *et al.* 1977). However, a number of studies, most notably Bogard & Tiederman (1986), Luchik & Tiederman (1987), and Tardu (1995), have observed further that several Q2 events often occur in temporal succession. In their words, a turbulent burst consists of multiple Q2 events. The hairpin vortex packet paradigm offers a simple explanation for this behaviour. Each Q2 is associated with a hairpin, and the clustering of the Q2s corresponds to the hairpins occurring in packets. The streamwise profiles in figure 13 are very similar to the temporal histories on which Bogard & Tiederman (1986), Luchik & Tiederman (1987), and Tardu (1995) based their work if Taylor's hypothesis is used to convert the streamwise coordinate to time.

Examples of hairpin packets at each Reynolds number are shown in figures 14–16. The convection velocity in these figures lies in the range 0.80–$0.82U_\infty$, and, in each figure, the vortex heads that convect at this velocity have been circled. Each circled vortex is associated with the usual hairpin vortex signature, and in addition, there are many other Q2 events associated with vortices that convect at different velocities,

such as vortex D in figure 14. In each vector plot, it is clear that a packet of hairpins occurs between the wall and the top of the logarithmic layer. Hairpin packets are observed most clearly, and hence most frequently in this region, probably because some of the vortices farther away from the wall are less intense, and therefore less readily visualized.

5.3. *Hairpin packets and zones of uniform momentum*

As noted in § 1, a remarkable feature of the turbulent boundary layer reported by Meinhart & Adrian (1995) is the fact that large, irregularly shaped regions of the flow have relatively uniform values of the streamwise momentum that are separated by thin regions of large $\partial u/\partial y$. (The term 'zones' was used to emphasize that these unsteady regions are defined in terms of instantaneous vector fields, in contrast to 'layers' such as the logarithmic layer that are defined in terms of average quantities and therefore have constant dimensions.) Analysis of the complete set of data studied here indicates that 75% of the PIV fields contain zones having these properties.

In figures 14–16 the uniform momentum zones have been separated by hand-drawn lines and labelled zones I, II and III. The lines pass through the centres of the heads of the hairpin vortices. With careful inspection, the region above zone II can often be subdivided into more than one additional zones, as in Meinhart & Adrian (1995), but for present purposes it suffices to recognize this fact without pursuing the details further. In the figures, the velocity vectors in zone II are small because their streamwise velocities are nearly equal to $0.8U_\infty$ while the velocity vectors in zones I and III have streamwise components of velocity that are significantly lower and higher than $0.8U_\infty$, respectively. The logarithmic layer contains both zone I and zone II. Contours of the u-component in figures 14(b)–16(b) provide a direct way of seeing the zones, and validate the hand-drawn boundaries indicated in the vector fields.

The coincidence between the heads of the hairpins and the boundaries between the zones of uniform momentum clearly demonstrates an association between hairpin packets and uniform momentum zones. This association is further substantiated by the data in figure 17 that show how the hairpin heads create regions of large $\partial u/\partial y$ along the boundaries between uniform momentum zones. In this figure, vertical profiles of streamwise velocity are superimposed on the $\partial u/\partial y$ contours. The streamwise component of velocity usually changes significantly between zones, but remains roughly constant within a zone.

Meinhart & Adrian (1995) suggest that the long region of uniformly retarded flow in each zone is the backflow induced by several hairpins that are aligned in a coherent pattern in the streamwise direction. The evidence presented here provides substantially deeper support for this interpretation, and it justifies extending the coherent vortex packet paradigm. In the extended view, the induced flow from each vortex adds coherently with the flows from succeeding vortices in a packet to create a region of low momentum that is significantly longer than the low-momentum region induced by any single hairpin. In this way, small structures (hairpins) combine to create structures that are long in the streamwise direction. As they grow, the packets also become large in the wall-normal and spanwise directions, but this growth is associated with the growth of individual hairpins, whereas the streamwise growth depends essentially upon the coherent alignment of successive hairpins. It should be emphasized that the alignment is not perfect, because the asymmetry of the initial hairpin leads to a meandering locus of the hairpins that are created subsequently (Zhou *et al.* 1999).

Packets may also align with other packets to create even longer zones. Therefore,

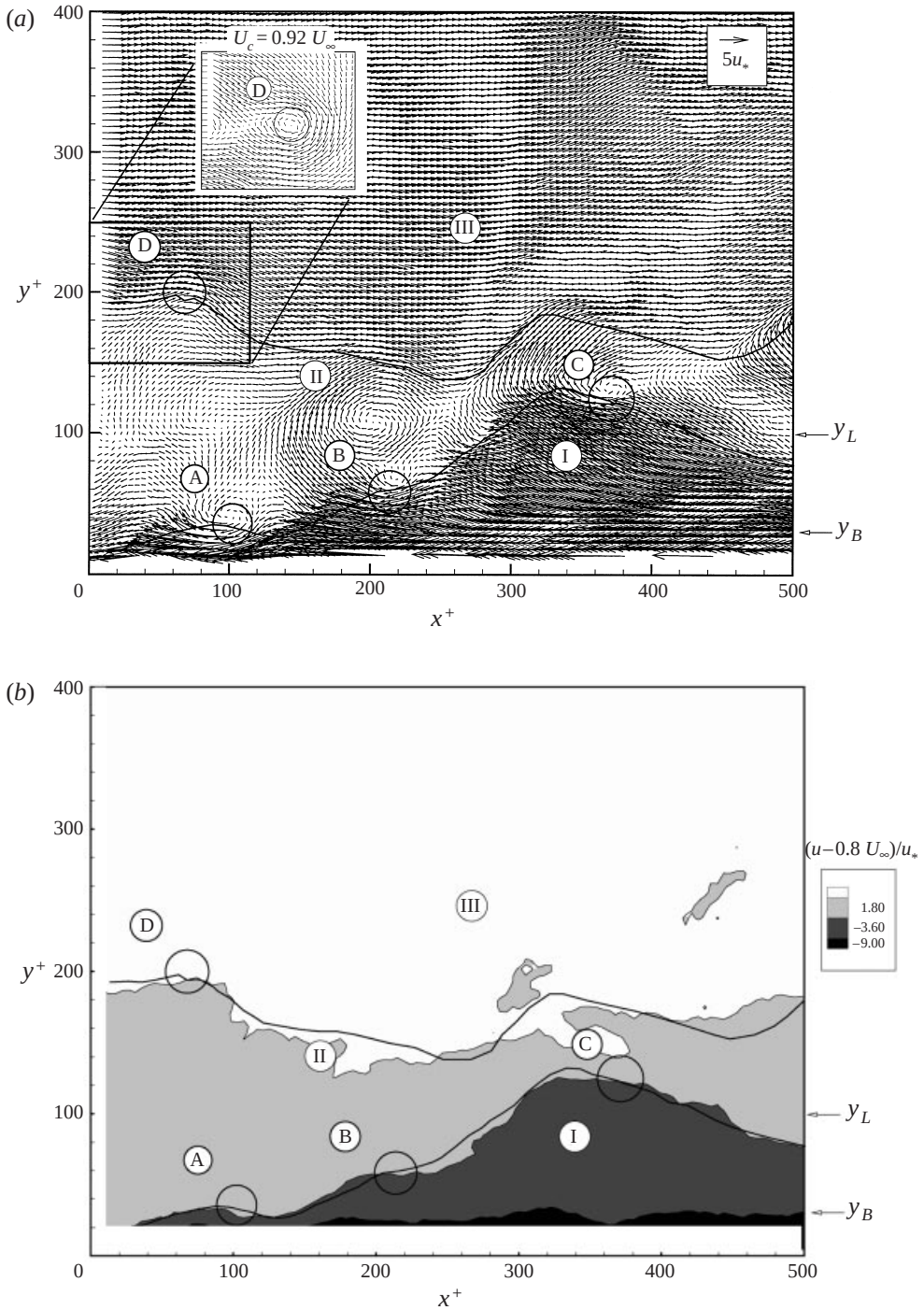

FIGURE 14. Realization of the $Re_\theta = 930$ boundary layer showing hairpin vortex heads along the boundaries separating regions of uniform-momentum fluid. The black lines separate the flow field into zones, labelled I, II and III, in which the streamwise momentum is nearly uniform: (*a*) instantaneous velocity vector map viewed in a convecting frame of reference $U_c = 0.8U_\infty$ and scaled with inner variables, (*b*) contours of constant *u*-momentum.

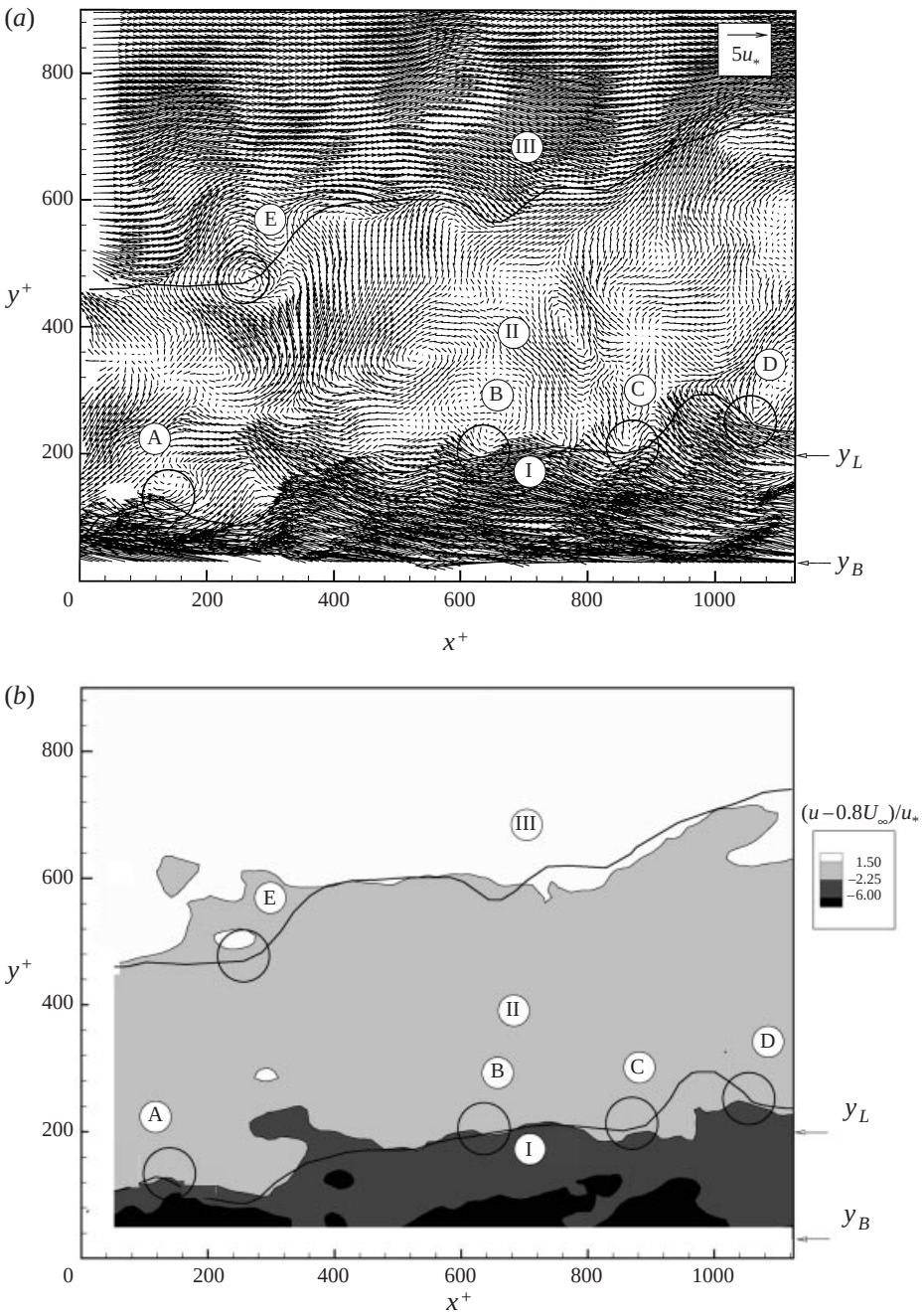

FIGURE 15. As figure 14, but $Re_\theta = 2370$.

a single zone of uniform momentum may be the manifestation of more than one packet. The low-momentum zones observed in this study extend far above the low-speed streaks observed in the buffer layer by Kline *et al.* (1967), and the evidence presented for low-momentum zones should not be confused with the older evidence for buffer-layer streaks. Note, however, that the buffer-layer streaks are a part of the low-momentum-zone phenomenon.

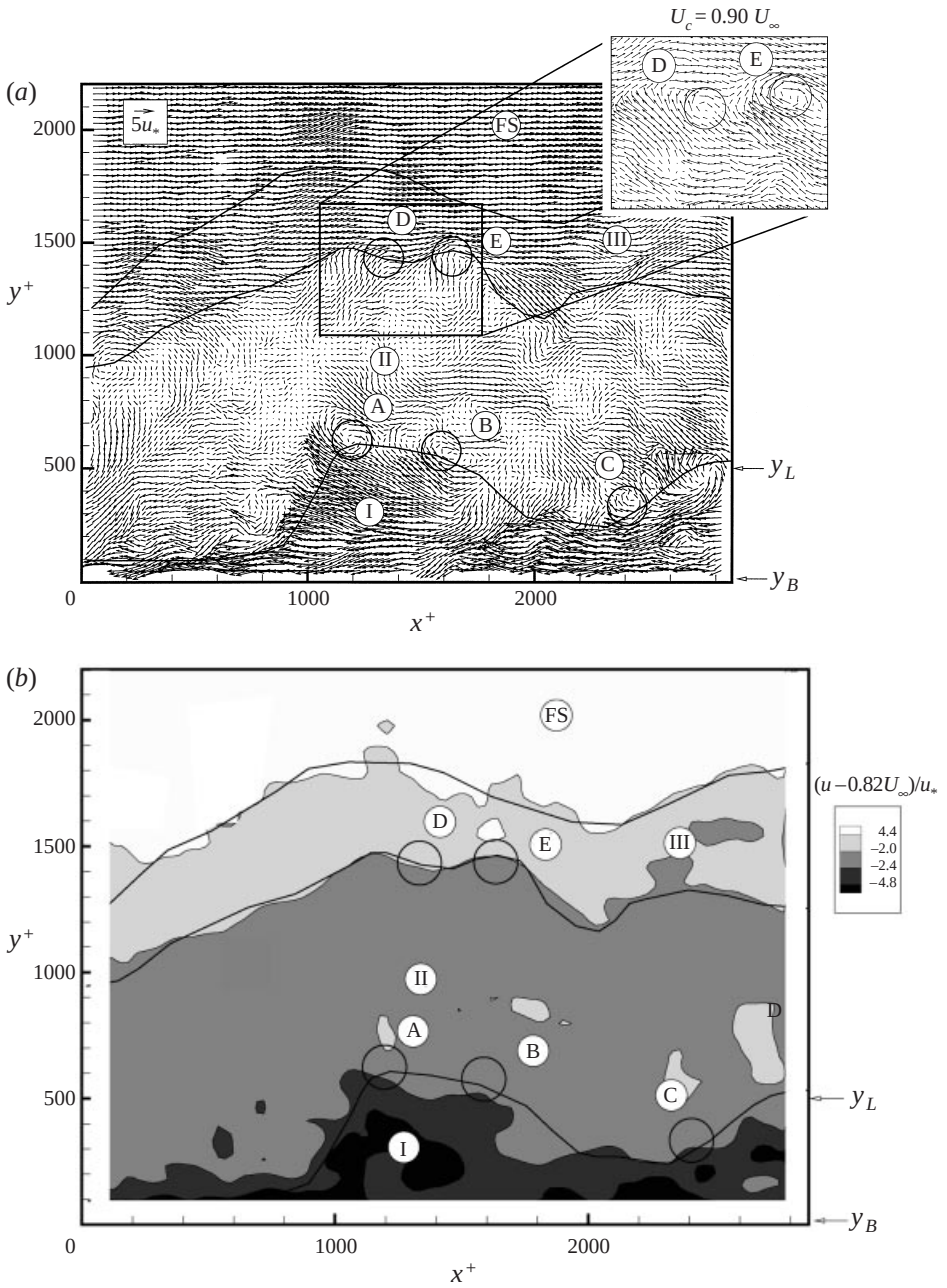

FIGURE 16. As figure 14, but $Re_\theta = 6845$.

The probability density histograms of the streamwise component of velocity found by accumulating the data over the entire area of each realization in figures 14(*a*)–16(*a*) are plotted in figure 18. Zones identified in figures 14–16 manifest themselves clearly in the form of local maxima of the histograms, each maximum being associated with a relatively narrow distribution of streamwise momentum that occurs in each zone. We refer to the distribution of velocities associated with each maximum as a *mode*,

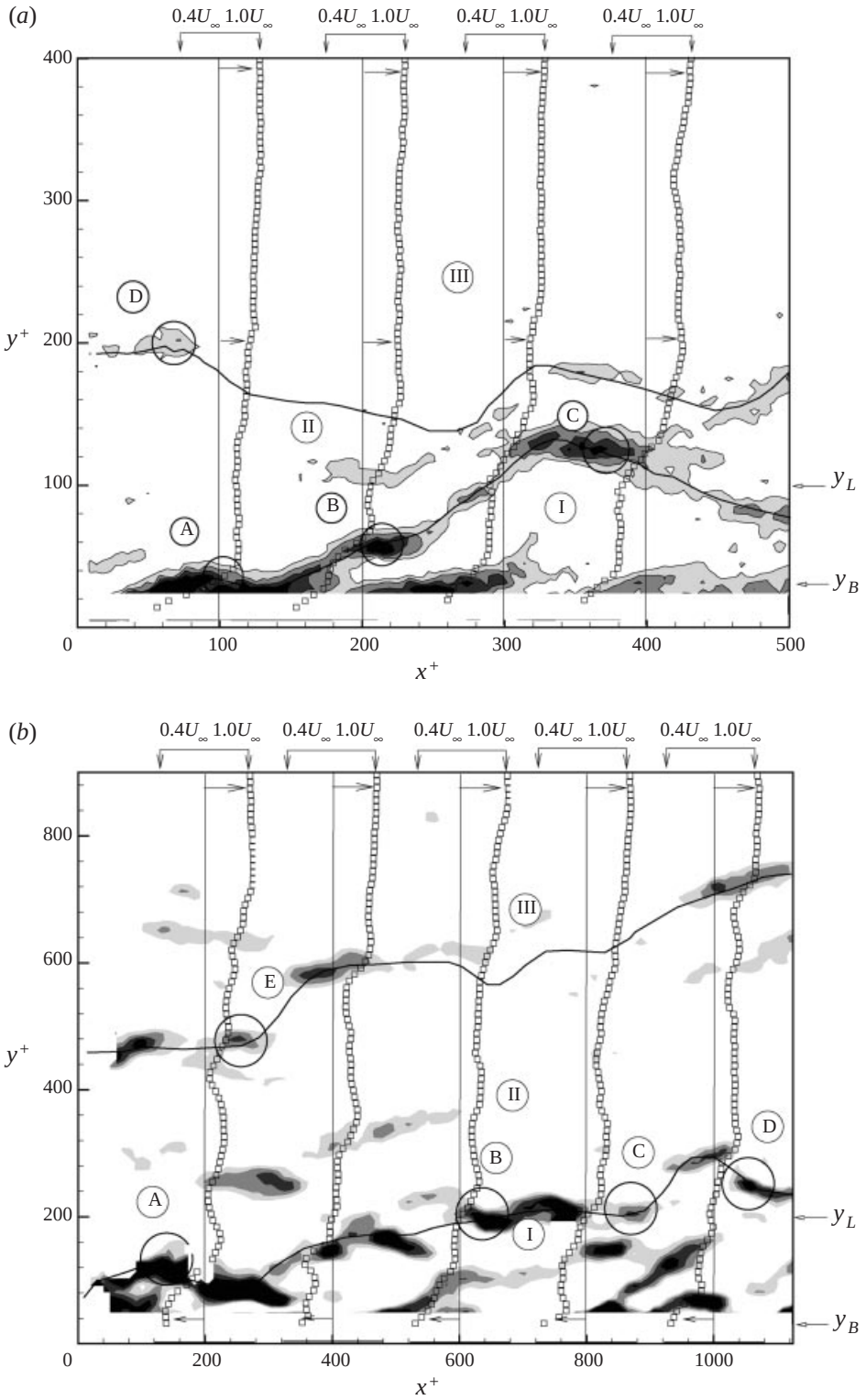

FIGURE 17(*a*, *b*) For caption see facing page.

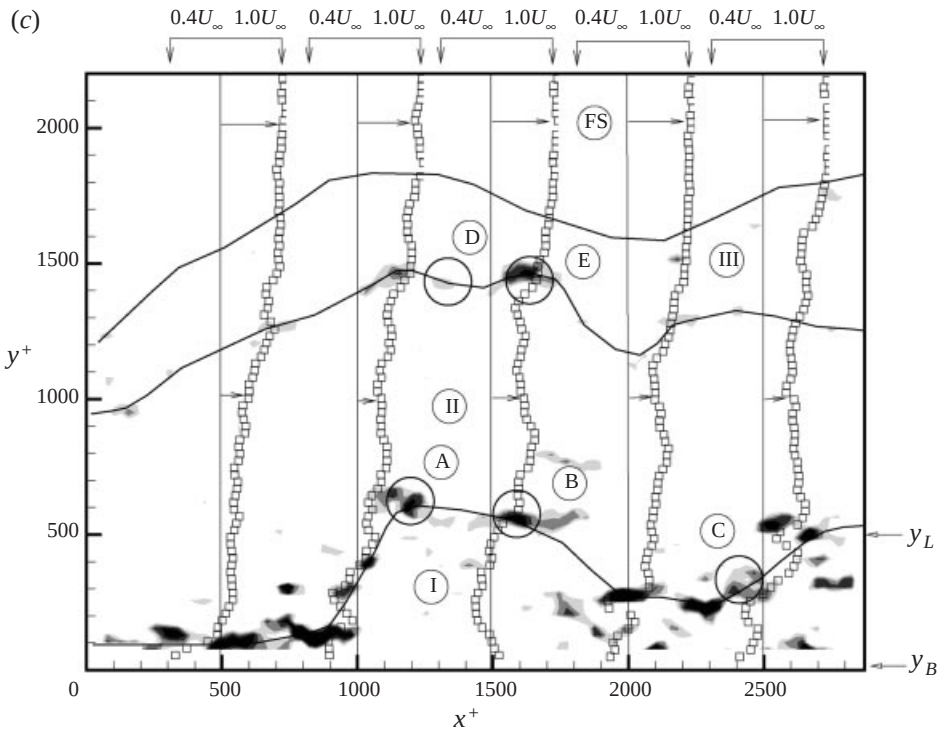

FIGURE 17. Zones of uniform momentum are separated by regions of large shear (contours are $\partial u/\partial y$) associated with the heads of the hairpin vortices. (*a*) $Re_\theta = 930$; (*b*) 2370; (*c*) 6845.

and the value of the velocity at which the histogram has a local maximum as the *modal velocity*. Many turbulence investigations have measured the probability density functions of fluctuating velocity. This type of measurement typically involves: (i) calculating the probability density function using Reynolds decomposed fluctuating velocity vectors; (ii) time averaging the probability density function over a long period; and (iii) averaging the probability density function at only a single wall-normal position. Any one of these standard operations tends to smooth the probability modes found by the present histogram analysis, rendering them unobservable. Reynolds decomposition subtracts that portion of the mean velocity that is, in fact, caused by momentum differences between the zones. To see this, observe how the Reynolds decomposed field in figure 9(*d*) removes the evidence of the uniform momentum zones. Ensemble averaging over many realizations smoothes because the maxima are located at different velocities from one realization to the next. Averaging over a long distance, or a long time, at constant y ultimately cuts through many zones and has the same effect as ensemble averaging. Thus, while the histogram analysis performed here is unconventional, it is a more useful means of extracting information about individual momentum zones than the conventional approach. It does, however, depend upon the extent of the field of view.

The modal maxima provide a quantitative method of describing the velocity in the various zones. To the extent that a zone in any given realization corresponds to a single packet of hairpins, the maximum may also be interpreted as the velocity within the envelope defined by the hairpin vortices. We shall see later that the hairpin packets have a mean length that exceeds the 1.2δ field of view of the present data.

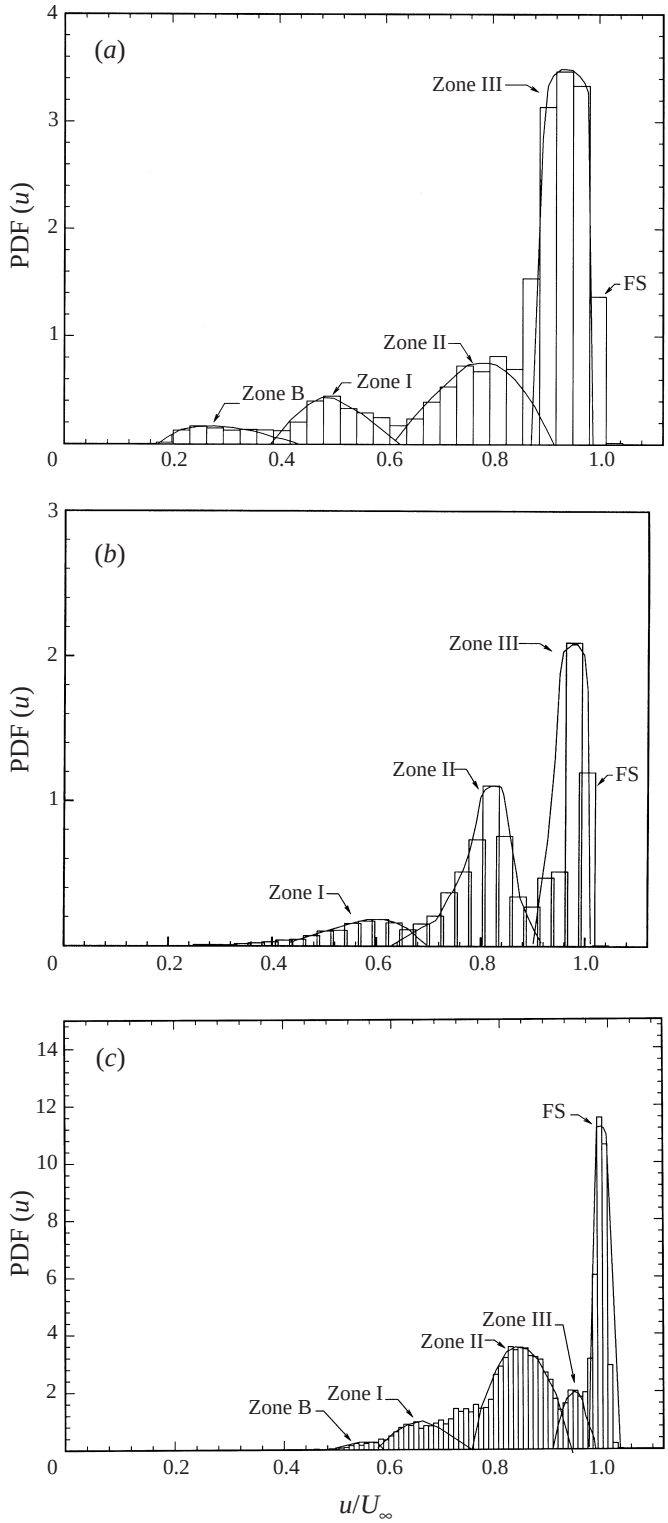

FIGURE 18. Histograms of the entire velocity field reveal modes associated with the uniform momentum zones. (*a*) $Re_\theta = 930$; (*b*) 2370; (*c*) 6845.

Re_θ	$\langle U_I\rangle/U_\infty$	$\langle U_{II}\rangle/U_\infty$	$(\langle U_{II}-U_I\rangle)/U_\infty$	$\langle U_I\rangle/u^*$	$\langle U_{II}\rangle/u^*$	$(\langle U_{II}-U_I\rangle)/u^*$
930	0.58	0.786	0.206	12.54	17.00	5.54
2370	0.60	0.80	0.201	14.37	19.19	4.82
6845	0.59	0.765	0.175	16.05	20.81	4.76
Average over Re_θ	0.59 ± 0.01	0.784 ± 0.02	0.194 ± 0.02	14.3 ± 1.7	19 ± 2.0	5.04 ± 0.4
Variation over Re_θ (%)	1.7	2.5	10	11.9	10.5	8

TABLE 3. Average modal velocities of zones.

Hence, on average, the data may include a portion of one packet and a different portion of another. Because of this, zonal velocities cannot always be associated with the induced velocities within a single packet, without some ambiguity. For example, in figure 18(*a*) the modal (i.e. most probable) velocities for Zones labelled B, I, II and III are $0.25U_\infty$, $0.48U_\infty$, $0.8U_\infty$ and $0.94U_\infty$, respectively. Since the velocity vectors from the free stream and zone III lay within the same modal peak, they are difficult to distinguish. The same difficulty appears in figure 18(*b*), but the modes are more readily distinguished in figure 18(*c*).

Zone B corresponds to the buffer region where viscous retardation causes a continuously decreasing velocity. Zones B and I combined correspond to the lowest-lying hairpin packets. (However, in figures 16(*a*) and 18(*c*) it is likely that the region labelled zone I actually contains vortices A and B that belong to a large packet – one of the ambiguities mentioned above.) Most commonly, the histogram modes associated with zones I and II are readily apparent for each Reynolds number. In terms of the hairpin packets, this implies that it is common for one hairpin packet (corresponding to zone I) to occur inside another (corresponding to zone II). Put the other way around, the existence of multiple zones of uniform momentum can be explained if, within the roughly $1.2\delta \times 1.2\delta$ field of view considered here, portions of two or more hairpin packets commonly coexist.

5.4. *Properties of near-wall packets*

Packets that lay within the first several hundred viscous wall units will be referred to as near-wall packets. This region contains Zones B and I. The hairpin packets studied by Zhou *et al.* (1996, 1997, 1999) are near-wall packets by this definition. The average streamwise spacing of vortex heads in this region is 104, 139 and 144 viscous length-scales for $Re_\theta = 930, 2370$ and 6845, respectively. These values are slightly smaller than the 165–220 viscous scale range found by Zhou *et al.* (1997, 1999) for the asymmetric hairpin vortex packet in channel flow. The mean spacing between successive hairpin vortices in Smith's (1984) laminar boundary layer was about 200 viscous wall units, which also coincides with the spacing of shear layer events in Tardu's (1995) boundary-layer measurements at $y^+ = 15$ and the spacing of pockets (Falco 1977, 1991).

For each Reynolds number there is a distribution of modal velocities found from the ensemble of realizations. The averages of the modal velocities $\langle U_I\rangle$ and $\langle U_{II}\rangle$ are tabulated in table 3. The average measured in zone I is $0.6U_\infty$ while the average for zone II is $0.78U_\infty$. The heads of the vortices that lie between zones I and II, i.e. the heads of the vortices in the near-wall packets, should propagate at approximately midway between these values, or about $0.69U_\infty$. Since the friction velocity is nearly proportional to the free-stream velocity over the range of Reynolds numbers studied

here, it cannot definitively be established whether the modal velocities scale with the friction velocity or the free-stream velocity, cf. table 3, but the evidence favours free-stream scaling. In fact, the values of $\langle U_I \rangle / U_\infty$ and $\langle U_{II} \rangle / U_\infty$ are remarkably constant.

6. Large-scale structure of the hairpin packets

The principal conclusion drawn from the foregoing section is that multiple hairpin packets commonly coexist, resulting in the appearance of multiple uniform momentum zones. Because of the limited streamwise extent of the data used in the preceeding section, it is not possible to determine the characteristic geometry of the packets, or to evaluate even simple properties such as their average length and height. Furthermore, the partial nature of the data leads to occasional ambiguities in the relationship between zones and packets. To resolve these problems, a second PIV experiment has been undertaken in which the streamwise field of view was increased from 1.2δ to 3δ by using lower-magnification photography (Tomkins 1997). Increasing the field of view of the PIV necessarily increased the interrogation spot size, i.e. it decreased spatial resolution. Consequently, the velocity data from this experiment, especially the vorticity data, are not as accurate as the measurements presented above. However, the data are sufficient to reveal the patterns of entire hairpin packets and to use the vorticity field for qualitative flow visualization.

Representative velocity fields from the $Re_\theta = 7705$ experiment are presented in figures 19, 20 and 23. The convection velocity subtracted from the flow vectors corresponds to the velocity of a middle zone in each figure. The solid lines are contours of constant u-velocity whose values were selected to coincide with the edges of the zones. In the expanded view of an inset the convection velocity is selected to coincide with the propagation velocity of the vortex heads, making them easier to identify. Vorticity contours in the expanded insets, indicated by grey-level contours, coincide well with the velocity vector patterns. Additional insets show highly idealized depictions of the zones and their boundaries. To improve the visualization of the vortex heads in figures 19 and 20, the kinematic swirling strength, instead of vorticity, has been plotted in the lower figure in the form of grey-level contours. Zhou *et al.* (1999) defined swirling strength as the imaginary part of the eigenvalue of the velocity gradient. It coincides with the vorticity when the vorticity is associated with roughly circular eddies, but it is negligible when most of the velocity gradient tensor is associated with pure shear. Thus, swirling strength discriminates against shear vorticity, making the swirling motion of a concentrated vortex core more obvious. For example, the vorticity contours plotted in the inset to figure 19 indicate extended regions of vorticity around $x/\delta = 1.5$ to 1.9, whereas the swirling strength indicates six roughly circular spots of high swirling strength in the same range.

The contours of constant velocity (solid lines) coincide closely with the locus of heads of the hairpins, as indicated by either local maxima of the swirling strength or the vorticity. The constant velocity contours provide a simple method of outlining a hairpin vortex packet. In figure 19 they clearly reveal three packets of hairpins containing uniform momentum zones labelled IIA, IB and IIB, whose heights increase downstream in an approximately linear fashion. Similar ramp-shaped uniform momentum zones are labelled IA, IIA, IB and IIB-IIIB in figure 20. This linear ramp pattern is a very common form of a hairpin packet, observed in 80% of the images for $Re_\theta = 7705$. Twenty-six per cent of the images contain two distinct inclines. The most probable length of a packet at the high Reynolds number is 1.3δ, and the maximum observed length was 2.3δ.

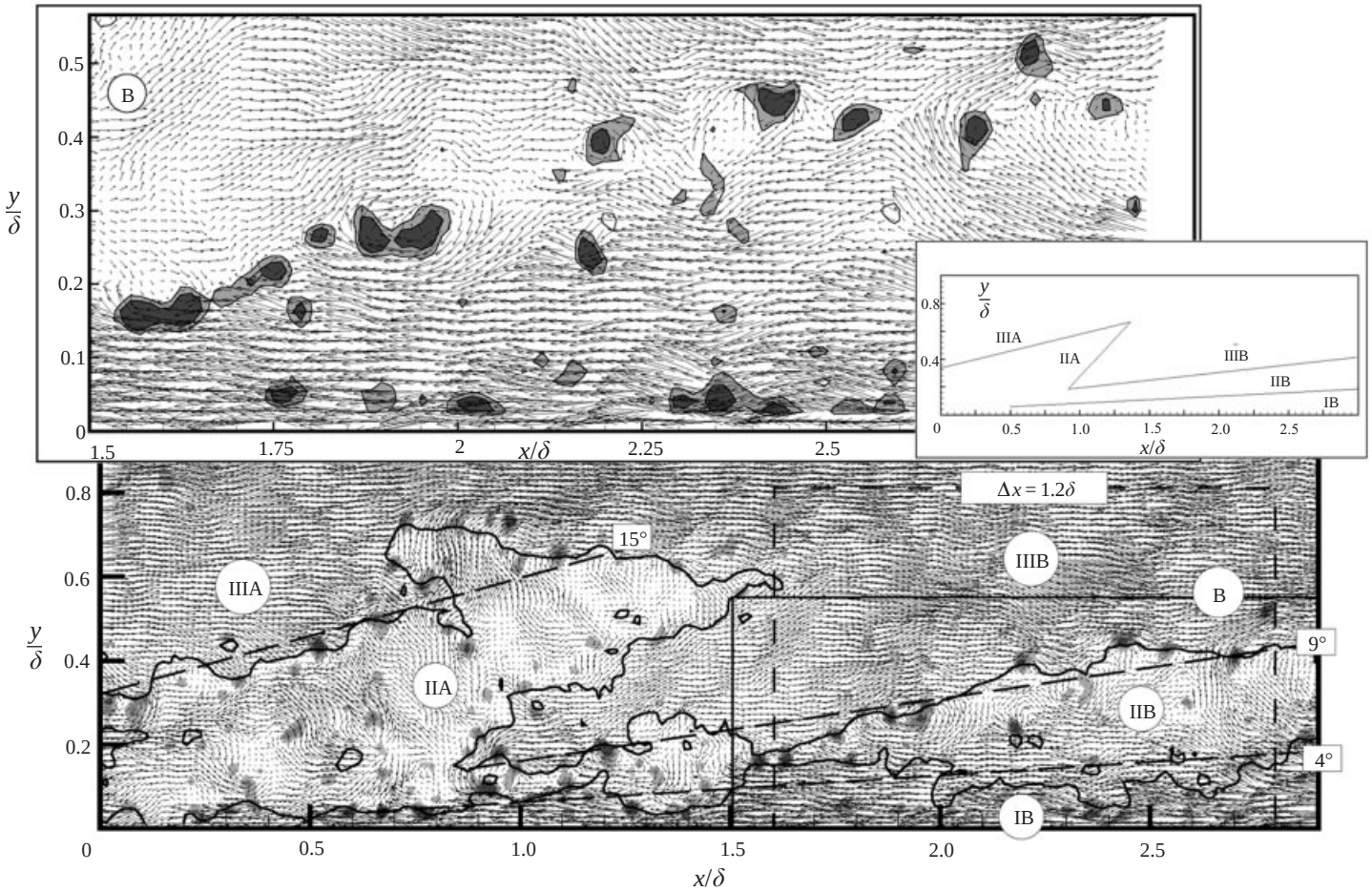

FIGURE 19. Illustrative example of large-scale structure of hairpin vortex packets at $Re_\theta = 7705$. The solid lines are contours of constant streamwise velocity at 61% and 79% of the free-stream velocity. The velocity field in the lower plot has $U_c = 0.75U_\infty$ subtracted and grey levels indicate swirling strength. The upper plot of the inset region B has $U_c = 0.75U_\infty$ subtracted, and grey levels indicate fluctuating spanwise vorticity.

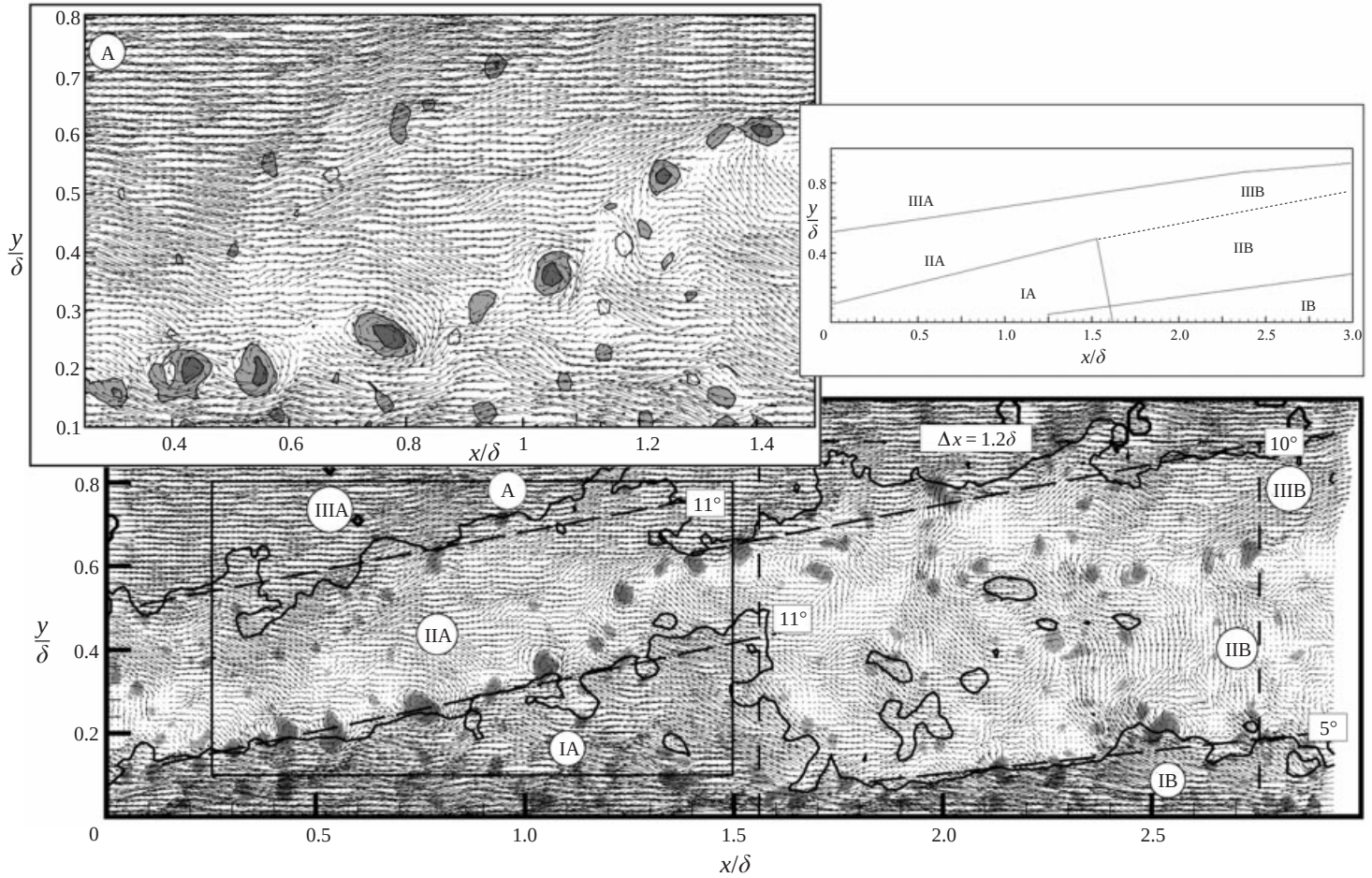

FIGURE 20. Second illustrative example of large-scale structure of hairpin vortex packets at $Re_\theta = 7705$. The solid lines are contours of constant streamwise velocity at 70% and 94% of the free-stream velocity. The velocity field in the lower plot has $U_c = 0.79U_\infty$ subtracted and grey levels indicate swirling strength. The upper plot of the inset region A has $U_c = 0.76U_\infty$ subtracted, and grey levels indicate fluctuating spanwise vorticity.

Figures 19 and 20 each show that small, presumably young, packets lying close to the wall (the near-wall packets) exist within larger, presumably older packets, which exist within still larger, still older packets. It is this mixture of packets of various ages and sizes that creates the multiple zone structure discussed in § 5. To illustrate the relationship, frames have been drawn in figures 19 and 20 (dashed lines) having widths of $\Delta x = 1.2\delta$, the same as in § 5. Viewing the restricted data within the frame gives a picture very similar to that developed in § 5.

Consider the IB region in figure 19. Along its upper boundary, which has a mean slope of 4°, there are at least 12 vortex heads, each about 0.03–0.05δ in diameter, evidenced by peak values of the swirling strength and ejection events. The IB region of uniform momentum thus lies within the cage formed by a packet of at least 12 hairpins, and it is caused by their combined back induction. The packet looks very much like the packets computed by Zhou *et al.* (1996, 1997, 1999), and sketched by Smith *et al.* (1991). The heads, and presumably much of the rest of each hairpin, travel downstream at about $0.61U_\infty$. This packet exists within the environment, labelled zone IIB, formed by the interior of a second packet that is more than twice as tall. That packet, in turn exists within zone IIIB, which may be the interior of a yet larger packet. (It is more difficult to identify packets in the wake region because the larger packets create weaker back-induced flow and the wake region is confused by the presence of the edge of the boundary layer.) The envelope of the packet that creates zone IIB grows at a 9° angle.

Upstream of packet IIB, in the region $0 < x < 1.5\delta$, another packet IIA forms a uniform momentum zone which includes at its bottom the near-wall packet that creates IB. It grows at a 15° angle, and it is taller than the packet that creates IIB. Packets IIA and IIB each move at about $0.79U_\infty$ (implied by the fact that the vortex heads fall on this velocity contour, and/or the interior induced flow zones have about the same velocity). Consequently, they must maintain a relatively constant streamwise position with respect to each other as they convect downstream. However, they must 'run over' packet IB, which is moving $0.18U_\infty$ more slowly. The consequences of such an encounter are expected to lead to a complex pattern of vortices owing to cut and connect processes and pairing processes.

The packets in figure 20 resemble those in figure 19 in many ways. Packets IA and IB propagate at nearly the same velocity, both lying along a velocity contour of $0.70U_\infty$, and both appear to be inside the back-induction zone IIA–B of a much larger packet. They have similar envelope angles, 5° close to the wall and 11° farther out, and the heights are comparable, 0.4δ for IA and 0.2δ for IB. Farther away from the wall, a series of vortices angle upwards, extending across almost the full view of the picture. These have been labelled packets IIA and IIB, and marked with growth angles of 10–11°, but they might also be interpreted as one long packet, as they both lay along the velocity contour corresponding to $0.94U_\infty$. Such a packet might be the result of a streamwise concatenation of two or more smaller packets. The above observations suggest the near-wall packets (IA, IB) and associated zones will propagate downstream together, remaining in close proximity, while the packets travelling above them (IIA, IIB) will be carried further downstream by the higher-speed outer flow, with a relative or dispersive velocity near $\Delta U = 0.24U_\infty$, the difference between the convection velocities. Similarly, it may be conjectured that higher-speed upstream structures currently out of the field of view may, at some later time, catch up with packets IA and IB (now slightly older and perhaps larger), potentially creating another complex encounter.

Upon further scrutiny, the layer structure in this realization may be yet more

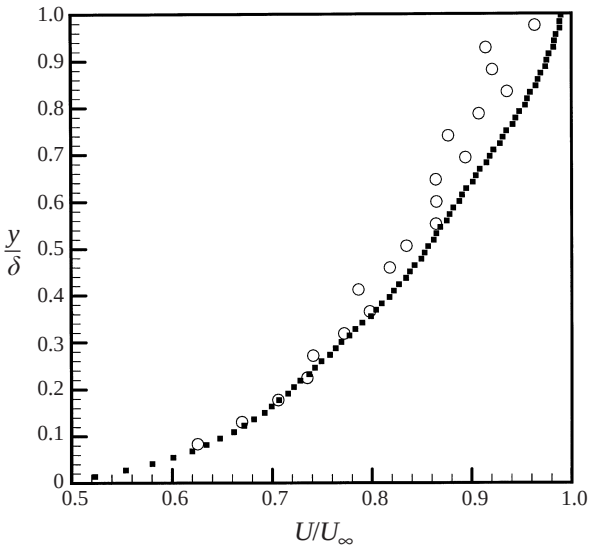

FIGURE 21. Conditionally averaged vortex streamwise convection velocities plotted as a function of wall-normal location at $Re_\theta = 7705$, ○, scaled with outer variables. ■, mean streamwise velocity profile.

complicated, because a sequence of hairpin heads, along the locus of the dashed line in the inset schematic, may indicate one more packet. Note that many regions of concentrated swirling strength and spanwise vorticity also occur in scattered locations without any obvious pattern. Thus, while the hairpin vortex pattern explains much of the flow, there is a non-negligible component of the flow that is more complex and less coherent.

The above realizations are examples in which the larger, presumably older, packets are convecting faster than the smaller, presumably younger, packets closer to the wall. This scenario is commonly observed in analysis of the data, and indeed turns out to be true on average. Figure 21 shows the convection velocities of all vortices in the $Re_\theta = 7705$ data as a function of wall-normal distance in comparison with the velocity profile. The convection velocities were calculated by conditionally averaging streamwise velocities at locations at which the swirling strength was both a local maximum and above a threshold. The threshold was set conservatively high ($\lambda_{ci} > 30\lambda_{ci,avg}$), i.e. the detection scheme may not have caught every vortex, but every conditionally extracted velocity measurement is likely to correspond to a vortex convection velocity. The velocities are then binned according to distance from the wall. The results are remarkably close to the velocity profile, consistent with the observations from figures 19 and 20. Scatter in the points further from the wall may be due to a smaller number of samples meeting the criteria at this location.

The scenario that emerges from the foregoing results is summarized schematically in figure 22, as viewed from the side in two dimensions. Here vortices are depicted in yellow, and the low-momentum regions induced by those vortices are grey, with darker grey corresponding to lower momentum due to stronger backwards induction by the surrounding vortices. It should be viewed as an idealization that refrains from attempting to portray the full complexity of real flows. The main features are:

(*a*) Packets consist of eddies that propagate together at packet convection speeds U_c.

(*b*) The angle of inclination of the hairpins in the packets is small close to the wall (quasi-streamwise vortices) and increases to 45–90° towards the head of the hairpin.

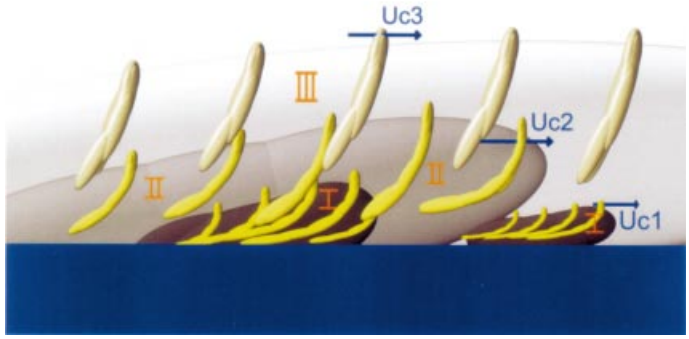

FIGURE 22. Idealized model of hairpin packets nesting within larger hairpin packets, and travelling at different velocities. The nested hierarchy creates the appearance of multiple uniform-momentum zones, and a progressively lower velocity as one approaches the wall.

(*c*) The packets have characteristic growth angles (defined by the angle of the envelope of the packet) that are smaller than the inclination of the heads.

(*d*) The most recently formed packets are small and propagate more slowly than the older, larger packets.

(*e*) Small packets exist within larger packets, and may be overtaken by the larger packets, so that the pattern of the flow is constantly changing.

In addition to the simple linear ramp structures, various other patterns have been observed. They include long, uninterrupted growth without zone II, an upstream ramp merging into a taller downstream ramp, and no ramp at all. However, in most cases when realizations display some type of pattern, that pattern contains a linear ramp angle in some form. For example, figure 23 illustrates a realization in which the near-wall low-momentum zone I contains both a positive and a negative ramp angle. Zhou *et al.* (1999) report the formation of hairpins downstream of the primary hairpin, leading to a negative angle consistent with that shown in figure 23. However, the flow in figure 23 contains several additional complexities. The realization exhibits a negative ramp angle above zone IIA followed by a positive ramp angle over zone IIB. Furthermore, immediately above the vertex of zone I a series of slight swirling patterns exist, which might be interpreted as being part of the hairpin packet in zone I, or an independent series of weaker structures. We have no solid interpretation of this pattern, and offer it mainly as a supplementary example to the scenario idealized in figure 22. Note, however, that even in this case the linear growth pattern occurs.

Although the details of the flow patterns are not the same from realization to realization, the regions of linear growth are a prominently recurring feature. Statistics on the growth angle have been gathered by fitting a linear curve to the edge of a low momentum zone wherever one occurred, independent of the distance from the wall. The resulting histogram, figure 24, shows that the most probable angle is 10.5°, with the angles ranging from 3° to 35°. The 12° mean angle agrees well with the simulations of Zhou *et al.* (1999). Some of the range of variation is due to not segregating the data according to distance from the wall, since the angle does tend to increase with y.

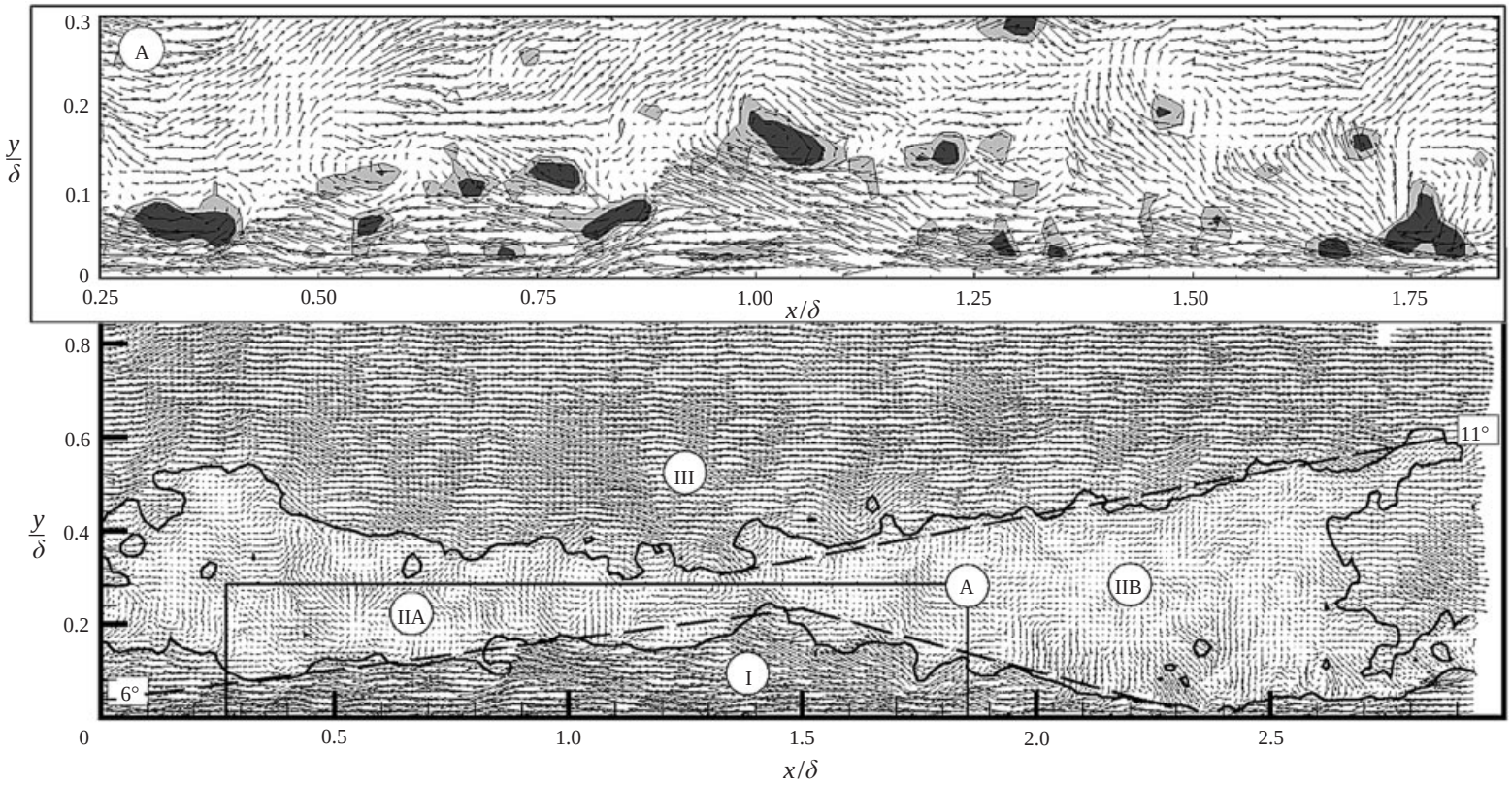

FIGURE 23. Example of a non-monotonically increasing hairpin vortex packet. $Re_\theta = 7705$, velocity contours at 70% and 76% of the free-stream velocity, lower plot $U_c = 0.79U_\infty$ and upper plot $U_c = 0.70U_\infty$, with grey-level contours of fluctuating spanwise vorticity.

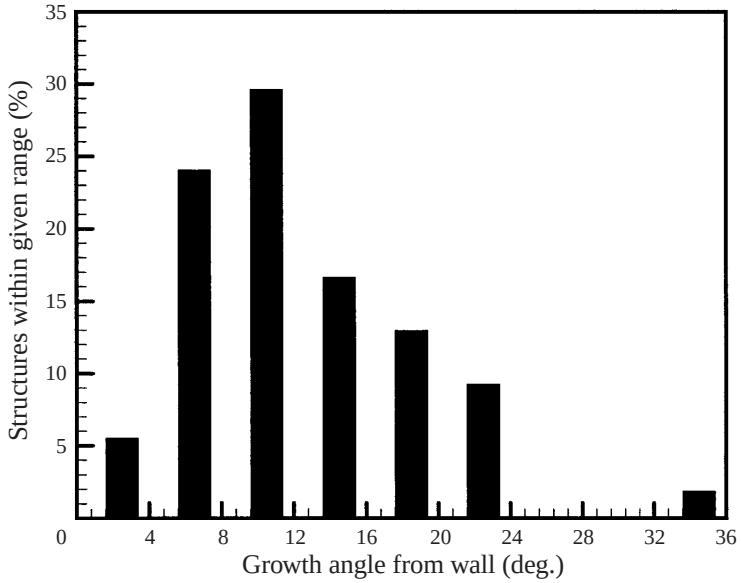

FIGURE 24. Histogram of the growth angle of linearly growing packets. $Re_\theta = 7705$.

7. Summary and conclusions

7.1. *Summary*

The structure of a zero-pressure-gradient boundary layer at three Reynolds numbers has been studied using PIV. Two separate experiments were performed: one with 1.2δ streamwise field of view and high resolution and one with 3δ field of view and correspondingly lower resolution. Single-point statistics measured by PIV in these flows agree well with available data from other investigations, indicating that the boundary layer behaved normally. The PIV measurements obtained with and without the boundary-layer trip showed that the trip did not change the overall structure of the boundary layer.

PIV data in the (x, y)-plane almost always contain several, usually many, hairpin vortex signatures. The signature is a two-dimensional velocity vector pattern characterized by (i) a vortex head with a Q2 event located beneath it along a roughly 45° locus, (ii) velocity vectors showing a maximum speed below the vortex head, and (iii) a shear layer caused by stagnation-point flow resulting from the Q2/Q4 interaction, cf. figure 10. The maximum in the speed of the Q2 event implies that the signature is caused by the combined induction of a three-dimensional vortex head and neck that surround the location of the maximum. A spanwise vortex could not produce a maximum. A simple inclined vortex in the (x, y)-plane could produce a maximum only if it were intensified by strong local stretching. A head and neck creating the concentrated induction is considered to be more probable.

In the outer layer, signatures of hairpin vortices are observed in all of the PIV realizations. The length of a typical signature close to the wall is about 200 viscous units, and the height ranges from the top of the buffer layer upwards. Close to the wall ($y^+ < 50$–100) (x, y)-plane patterns of ejection are consistent with the vortex legs bending and becoming quasi-streamwise vortices. The angle θ at which the neck and head are inclined to the wall varies from 15° to 75° (with 45° being typical), as determined by the angle of the signature shear layer. It is consistent with the range

of angles observed from the quasi-streamwise vortices to the hairpin head in Zhou *et al.* (1999). The angle of the hairpin head is a strong function of its location; the head takes a near vertical orientation in the outer regions of the boundary layer, while near the wall it takes a more conventional 25–45° angle. The length and height increase with y, presumably as the hairpin grows in time.

The three-dimensional pattern of a real hairpin is neither symmetric nor deterministically reproducible, but despite random variations, its imprint on the two-dimensional velocity field is easily recognized. The quasi-streamwise vortex pattern, the hairpin shape, the horseshoe or omega shape, and the one-sided cane-type vortices are all part of the same entity at various stages of their evolution, with different aspect ratios and different degrees of asymmetry. We refer to this entity in any of its forms as the 'single hairpin paradigm'. This paradigm has a long history, but despite several notable pieces of pioneering work supporting the concept, it has not enjoyed unequivocal acceptance. Theodorsen's (1952) horseshoe vortex founded the hairpin-vortex paradigm, although it failed to countenance quasi-streamwise legs. The visualizations of Head & Bandyopadhyay (1981) made a strong inferential case for hairpins, but the uncertainties of smoke visualization, the use of a large sawtooth boundary-layer trip and the rarity of clear observations of individual hairpins left the question open to debate. Praturi & Brodkey (1978) saw all of the elements of hairpin vortices, but an entire composite hairpin was not observed. Likewise, Robinson's (1991, 1993) direct numerical simulation study of boundary-layer structure identified all of the parts of a hairpin structure, but stopped short of unqualified endorsement of the hairpin paradigm, presumably because clear examples of a complete hairpin were rare using the visualization tools available (three-dimensional contours of vorticity and pressure). Recently, the evidence for hairpin vortices similar to the paradigm sketched in figure 10 has begun to accumulate for low-Reynolds-number flow. Chacin, Cantwell & Kline (1996) achieved clearer visualizations using critical-point analysis of DNS data for fully turbulent channel flow. The numerical simulations of Zhou *et al.* (1999) and Singer & Joslin (1994), and the experiments of Haidari & Smith (1994) and Smith *et al.* (1991) all lend credence to hairpin formation in low-Reynolds-number flows, although none of these flows were turbulent.

The evidence presented here is believed to be the first experimental study that offers strong quantitative support for the existence of hairpin vortices in relatively high-Reynolds-number wall turbulence. It cannot be disputed that hairpin vortex signatures populate the boundary layer abundantly. They are found everywhere if looked for either using (x, y)-plane flow patterns in frames of reference that travel with the vortex heads, or using swirling strength, which discriminates against the shear vorticity in favour of the swirling component of vorticity. If the relatively credible hypothesis that the hairpin vortex signature, as defined, is a manifestation of a hairpin vortex is accepted, then it must be further concluded that hairpin vortices populate real boundary layers abundantly at both high and low Reynolds numbers.

Beyond the existence of hairpin vortices, the data also show individual hairpins commonly aligned behind each other in the x-direction to form a group. The groups, or 'packets' propagate with small velocity dispersion (approximately 7%), such that the relative spacing and arrangement of the hairpins within a packet remain coherent for long times. More than 10 hairpins have been observed per packet, and packets may extend out to 0.8δ and be as long as 2δ. These packets are the dominant flow structure from the outer edge of the buffer layer to the outer wake region at each Reynolds number.

In the most commonly observed configuration of a packet, the envelope of the

packet, as observed in the (x, y)-plane, is a linearly growing ramp. This remarkably linear structure is observed more frequently in high-Reynolds-number flow than in low-Reynolds-number flow. The linear hairpin packet paradigm is a fair representation over a range of Reynolds numbers, but the structures are not so linear at the lower Reynolds number. Observations in the lower part of the outer layer, i.e. $y^+ < 200$ are generally consistent with Smith's (1984) observation of multiple hairpin formation in wall turbulence at low Reynolds number, and they mutually support the basic theory of near-wall hairpin formation by the viscous/inviscid mechanism (Smith *et al.* 1991), and the low-Reynolds-number numerical simulation of Zhou *et al.* (1999). These are the packets in their early stage of growth, associated with uniform momentum zone I. Like the near-wall packets, linear ramp-shaped packets have also been observed to form the outer edge of the boundary layer (Bandyopadhyay 1980).

The second principle contribution of the present work is to show that hairpin packets occur throughout the boundary layer, often one within another, and at various stages of growth. These observations of packet structures internal to the boundary layer complete a picture in which packets are created at the wall and grow to span a significant fraction (sometimes all) of the boundary layer. The internal packets have not been sensed by previous investigations using smoke visualization or H_2-bubble visualization, presumably because of small-scale turbulent dispersion within the boundary layer. The present work also shows that zones of relatively uniform streamwise momentum exist within the packets. The nesting of one packet within another leads to the creation of multiple zones of different uniform momentum.

Lastly, inspection of the contour plots of spanwise vorticity and the swirling strength both reveal vortex cores throughout the boundary layer whose diameters are approximately constant and close to the diameters of the cores located near the wall. Larger cores also exist, but they are harder to see than the smaller, more intense cores. The diameter of this 'smallest' vortex may not scale with either inner or outer units, but, typically, it is 30 viscous wall units.

7.2. *Structural model*

The hairpin packet paradigm has the potential to unify many seemingly unconnected, or even disparate facts about the structure of turbulent boundary layers. The rest of this paper will be directed to understanding the current body of wall turbulence lore in the context of hairpin packets. To this end, we will first describe an idealized conceptual model based on the hairpin packet paradigm, and then show how it explains most facts known about coherent structures in the outer region of wall turbulence. The model is derived mainly from the combination of results from Zhou *et al.* (1999) regarding the initial formation and growth of the hairpin packet, and the present experimental PIV results regarding hairpins and hairpin packets in higher-Reynolds-number flow. It rests squarely on the pioneering contributions of Head & Bandyopadhyay (1981) and Smith and co-workers, although much of the hairpin packet concept was developed along independent lines until Tomkins' (1997) experiment incontrovertibly showed packets in the linear ramp-form depicted by Head & Bandyopadhyay (1981). Also, we only recently became aware of a model proposed by MacAulay & Gartshore (1991), which also includes the hairpin packet concept. None of these studies, including ours, dealt with interactions between hairpins or hairpin packets, so all effects due to interactions are absent.

It is assumed that the mechanisms for hairpin vortex autogeneration studied at low Reynolds number in the channel-flow simulation of Zhou *et al.* (1996, 1999) also pertain to the low-Reynolds-number region of high-Reynolds-number boundary

layers. That is, the DNS calculations, which extend up to $y^+ \sim 150$ at the centreline of the channel represent the hairpin evolution that occurs in the first few hundred viscous lengthscales of a much deeper high-Reynolds-number boundary layer. Subsequent evolution and generation within this deeper layer lead to the observed increases in number of vortices per packet and streamwise length in terms of viscous wall units. Differences between flows in channels, boundary layers and pipes are assumed to reside mainly in the large scales, of the order of the scale imposed by the boundary condition. Although the large scales may have some effect on the growth of the small scales, their effects will be ignored, until future work can provide better evidence about them.

In this model, packets originate at the wall from a disturbance whose character is not specified except that it creates a pool of low momentum at the wall, i.e. a Q2 event from another hairpin, a bump, a puff of low momentum through the wall, a random pressure fluctuation, or a culmination of flow induced by surrounding events such as wall-tangent flows that converge to a stagnation point and thence erupt upwards. First, the primary hairpin is formed. It is stretched and intensified by the difference between the streamwise velocity at its legs and its head, and grows continuously in time, changing from a hairpin-shape to an omega-shape. If its strength is sufficient, it autogenerates a new upstream hairpin by inducing a strong, three-dimensional Q2 that interacts with high-speed fluid behind the primary hairpin. As time progresses, the secondary hairpin increases in size and, at a certain time, it, too, begins to create a tertiary hairpin. The angle of the envelope connecting the heads of the hairpins, γ, is determined by (i) the rate of continuous growth vertically (and spanwise), (ii) the streamwise convection velocity of the hairpin, and (iii) the relatively uniform time between the formation of successive hairpins. The primary hairpin is also capable of generating a new hairpin downstream of the primary, and this hairpin may generate others (Zhou *et al.* 1999). Unless the initial disturbance is smooth and perfectly symmetric about the (x, y)-plane, the resulting packet of hairpins is not symmetric, and, at later times, the pattern of vortices in the packet becomes quite complex (Liu & Adrian 1998), even in a clean background flow at low Reynolds number. Even so, the characteristic growth angle γ, can usually be discerned, implying that the growth rate is not sensitive to the geometric details of the vortices. In a real turbulent flow, a new packet forms in an environment of larger-scale random flow that will increase randomness in the packet. Thus, linear growth is not always observed in the experimental data, nor is the growth rate constant. However, for the purposes of an idealized model, it seems reasonable to assume that the packets grow linearly, albeit with different rates.

The idealized packet is a ramp or diamond with a growth angle γ (see figure 25). The young hairpins are about 100–200 viscous wall units apart, and their legs are about 50 viscous units apart. In the buffer layer, low-speed streaks form between the legs. The spacing of 100 viscous wall units between low-speed streaks indicates that the young hairpins are densely distributed on the wall. The computations of Zhou *et al.* (1999) show that the legs spread in the spanwise direction as the hairpins age, which we assume is also true for large Reynolds numbers. This is one of the few major departures from the concepts of Head & Bandyopadhyay (1981), who suggested that the mean spanwise width of the hairpins was 100 viscous units from the wall to the top of the boundary layer. In our view, such narrow structures would be shredded by the motion of larger eddies. One cannot, for example imagine 1 mm wide hairpins stretching from the earth's surface to the top of the planetary boundary layer. The basis for Head & Bandyopadhyay's (1981) thin hairpin model was the observation of occasional hairpin loops of smoke at the upper edge of the boundary layer having

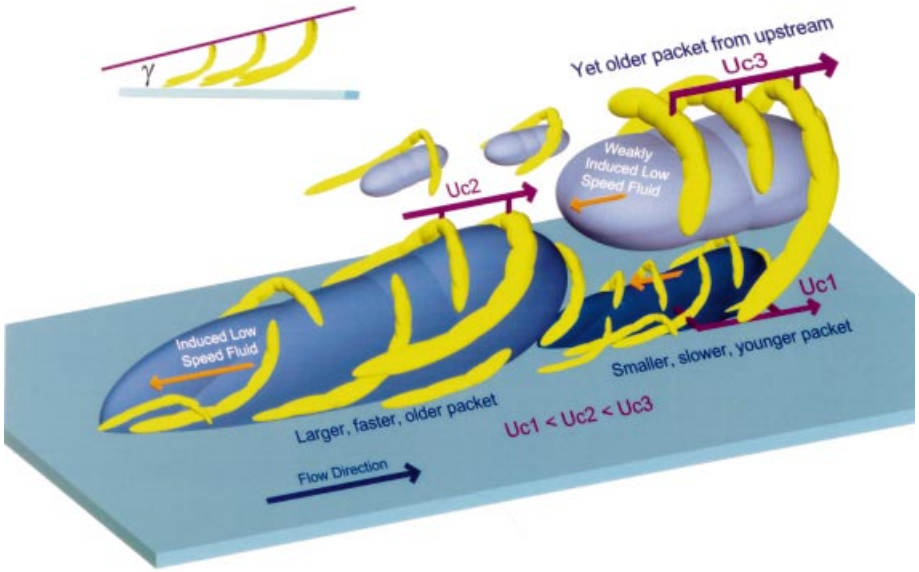

FIGURE 25. Conceptual scenario of nested packets of hairpins or cane-type vortices growing up from the wall. These packets align in the streamwise direction and coherently add together to create large zones of nearly uniform streamwise momentum. Large-scale motions in the wake region ultimately limit their growth. Smaller packets move more slowly because they induce faster upstream propagation.

widths of the order of 100 viscous units. However, narrow hairpins in this region could also be explained by assuming that they were formed locally, i.e. at the top of the boundary layer and not at the wall.

The convection velocity of a vortex in a packet is determined by the velocity of the environment in which the vortex exists and the velocity with which the vortex propagates though that environment owing to mutual induction of its elements and the elements of the surrounding vortices. To first order, we can approximate the streamwise convection velocity of the head and neck of a hairpin by the velocity of the surrounding fluid minus the upstream component due to self-induction, proportional to the circulation of the vortex core divided by the width (or diameter) of the hairpin. According to this model, the larger hairpins have a smaller back-induced velocity, and hence propagate downstream more rapidly. In a young packet with only a few hairpins having nearly the same size, this means small velocity dispersion, and relatively slow downstream convection speed. As a packet ages, its larger hairpins begin to move downstream at a significantly faster rate than the smaller, younger hairpins, in part because the back-induced velocity decreases with increasing size and in part because the background flow may be faster at greater distances from the wall. The packet becomes stretched as the larger, older hairpins move away from the younger, smaller hairpins, and on average, larger packets move more rapidly than smaller packets.

The hairpin packets are also related to bulges in the outer surface of the boundary layer. At low Reynolds numbers the packets contain fewer hairpins than in higher-Reynolds-number flow, so a typical packet may contain 2–3 vortices. Packets that grow to the outer region define the instantaneous boundary-layer edge, which is highly corrugated at lower Reynolds number, and are the previously observed turbulent

bulges. The length of the bulges is known to be about 2δ (Kovasznay, Kibens & Blackwelder 1970), while the distance between hairpins scales roughly with viscous wall variables at about 100–200 viscous wall units. Hence, the number per packet increases with increasing Reynolds number. The scaling of distance between hairpins is not simple, in part because the distance increases as the hairpins grow.

When considering hairpins attached to the wall, there appears to be an upper limit on their height $\sim 1.2y_L$, for all three Reynolds numbers. This implies that outer variables govern the upper limit on hairpin head heights. The overall dynamics of hairpins does not appear to be governed by just inner or outer variables. The mechanism responsible for the streamwise spacing may be governed by inner variables for the larger Reynolds numbers. If these heads are related to bursts in the buffer regions, then the streamwise spacing may be related to burst frequency, which has been investigated by numerous researchers. Many of these researchers have reported that burst frequency scales with inner variables, including Blackwelder & Haritonidis (1983), Kim & Spalart (1987), Luchik & Tiederman (1987) and Wark & Nagib (1988). The concept of burst frequency scaling with inner variables is consistent with the concept of average streamwise spacing scaling with inner variables.

Figure 25 portrays three hairpin packets, each formed from 3–6 asymmetric hairpins whose vortex cores are shown in yellow. The vortices are depicted here with a moderate degree of asymmetry, though for any given vortex this may vary from nearly symmetric to highly asymmetric (one-sided or cane-like). The cores of the hairpins grow with increasing distance from the wall, but less strongly than outer scaling would predict, and the larger packets have larger hairpins, and, hence, faster convection velocity, U_c, in the streamwise direction. The younger packets are comprised of attached eddies. On the basis of the available data, we are unable to say whether the legs of the oldest, largest packets are attached to the wall, in the sense that they extend down to the wall, or whether they are analogous to the type B eddies of Marusic & Perry (1995), which are physically detached but 'attached' in the sense that their size scales with distance from the wall. Note also the depiction of two smaller detached hairpins in the outer flow. The appearance in the data of smaller HVS in the outer region suggests hairpins may be formed locally away from the wall, consistent with the observations of Rogers & Moin (1987) in homogeneous shear flow. Within each packet, the flows induced by the vorticity of the cores of the hairpins combine to form an interior region having relatively uniform streamwise momentum (indicated in blue). The back-induced flow is proportional to the core circulation divided by the diameter of the hairpin, like the induced propogation. Hence, smaller packets have stronger back-induced flow (darker blue), and the smaller end of a packet has stronger back-induction than the larger end. The induced momentum is not uniform, because back induction varies as hairpins grow, and since the growth angle γ is small, the momentum is slowly varying. Thus, the streamwise velocity in a zone of uniform momentum is constant only in an approximate sense.

The streamwise alignment of the hairpins in a packet is not perfect, and the evidence of waviness in the low-speed streaks in the buffer layer suggests that the hairpins may be displaced laterally by as much as the spanwise width of the hairpin over the length of several hairpins. Even so, the hairpins are relatively well aligned for long distances, as evidenced by the fact that packets have been observed containing more than 10 hairpins. We refer to this as 'coherence' between the hairpins in a packet, meaning that there is an organized pattern of hairpins in space. Because of this coherence, the back-induced flows from the hairpins combine to produce stronger backflow than could be achieved by incoherently aligned individuals. The flux of

fluid in the streamwise direction is analogous to the magnetic flux induced by current flowing through windings of an electromagnetic solenoid. For this reason, we shall refer to the intensification of the back-induced flux by the hairpin coherence as the 'solenoid' effect. Clearly, more windings or closer spacing imply more flux.

The appearance of multiple zones of uniform momentum is a consequence of older, larger packets over-running smaller, younger packets. Thus, a region labelled zone I in the earlier discussion corresponded to the interior of a young packet, while the region labelled zone II corresponded to the interior of an older packet. The small end of a large, old packet could be labelled zone I, while its large end could be labelled zone II, or even zone III, if two smaller packets lay beneath it. Thus, the instantaneous configuration of packets determines the pattern of the zones of uniform momentum. Since the packets move with different velocities, the pattern is ever evolving. This could explain why wall turbulence can look very complicated, even if it is made of relatively simple elements.

When a new packet grows inside the uniform momentum zone of an older packet, it experiences a flow environment different from the free stream. The velocity differences are less, and, hence, it is strained less. In this way, small packets are shielded from the full straining potential of the boundary layer. As the packets grow, the velocity differences between adjacent zones should decrease.

The model implies that turbulence structures arise at the wall, and grow by continuous straining of the hairpins, coupled with mutual induction interactions within the packets. This is one fundamental means by which the lengthscale increases linearly with distance from the wall. It also implies that large structure in the turbulent boundary layer is created by coherent concatenation of hairpins, as well as growth of the hairpins by straining. These large structures may grow well beyond the logarithmic region. While the creation of large eddies from small eddies appears at first blush to run counter to the energy cascade process, it must be remembered that the inhomogeneity of wall turbulence permits this to happen. Furthermore, it is conceivable that the large structures can become unstable and break down into smaller eddies, even though they were formed from small eddies. The model says little about interactions of packets because the evidence about such interactions is not openly available. Yet, unpublished simulations in our group indicate that interactions do occur. Lateral interactions produce a vortex annihilation in which the right leg of the hairpin in the left packet annihilates the left leg of the vortex in the right packet, cf. Wark & Nagib (1989). The remainder is a double-wide vortex and a low-lying counter-rotating vortex, if the remaining quasi-streamwise vortex segments reconnected viscously. The double-width vortex produces half the back-induced motion, which might account for the region marked IIb in figure 20. This is a second mechanism for growth of the turbulence lengthscale.

The full range of hairpin and hairpin packet interactions can only be speculated. They range from soliton behaviour in which packets pass through other packets without lasting modification, to pairing by vortex interaction, to total disruption of the ordered structure by many vortex cuts and reconnects. The latter seems the least likely, because it would result in relatively few old packets, contrary to observation. However, the cut and reconnect mechanism should occur to some extent, and it may be effective in the wake region of the boundary layer where packets are infrequent.

7.3. *Discussion and conclusions*

Although it is conceded that a full picture of the structure of the turbulent boundary layer requires an understanding of the interaction of hairpins and packets, and

perhaps the discovery of structures that have not yet been observed, the simple model presented above is capable of explaining much that is known about the structure of wall turbulence. Below we list all the important features that can be explained on the basis that the boundary layer is made up of hairpin packets.

The single hairpin vortex paradigm by itself explains many aspects of structure in the turbulent boundary layer. Robinson's (1991, 1993) observations that quasi-streamwise vortex legs dominate the buffer layer, inclined necks and heads dominate the logarithmic layer, and that heads are predominant in the outer layer are consistent with a distribution of hairpins having different sizes. Ejections (Q2 events) in the outer layer can be associated with the flow induced by the head and neck. Low-speed streaks in the buffer layer can be attributed to low-momentum fluid lifted up by the induction of the quasi-streamwise vortices. The results Sirovich (1997) obtained from proper orthogonal decomposition (POD) of low-Reynolds-number channel flow show that the most important POD modes are the streamwise independent modes with support close to the wall and a pair of inclined propagating modes with support in the core. The former modes can be attributed to the quasi-streamwise legs of the hairpins and the associated long, low-speed streaks. The propagating modes that trigger the onset of burst-like activity can probably be attributed to projections of the hairpin heads onto propagating POD modes.

However, the single hairpin paradigm does not account for certain essential features. Numerical simulations indicate that the length of a single hairpin can only account for streaks and ejections that are several hundred viscous wall units long, considerably shorter than observations. Also, a single hairpin cannot explain the formation of long streaks of low-momentum fluid in the outer layer, as observed by Chen & Blackwelder (1978), and more explicitly by Meinhart & Adrian (1995), nor can it explain the occurrence of ejection events in groups.

The hairpin vortex packet paradigm provides an explanation for these phenomena and others. In the buffer layer, cooperative second-quadrant pumping of the near-wall fluid by the legs of many streamwise-aligned hairpin vortices in a packet can create very long (more than 1000 wall units) low-speed streaks. The tendency of packets to form as a spanwise-staggered array of one-sided hairpins can explain the often-observed slow spanwise oscillation of the low-speed streaks.

Low-speed streaks are observed in the outer layer as well as in the buffer layer. Also, the time-delayed u-autocorrelation function is known to possess a long tail, indicating structure that is very long (of the order of δ or more) in the streamwise direction (Grant 1958; Townsend 1958). These structures are Townsend's (1976) large-scale inactive motions. We interpret them to be consequences of the coherent induction of the hairpins in a packet. The low-speed streaks associated with individual vortices are only a few hundred viscous wall units long (Zhou *et al.* 1999), so the alignment of many such vortices is necessary to explain the large-scale structures. This coherence is more effective for the streamwise component than for the wall-normal and spanwise components because of the streamwise alignment of the vortices. Hence, the correlation length of the streamwise velocity is much longer than the correlation length of the other two components. The individual vortex members contribute to the Reynolds stress and wall-normal turbulence locally, owing to the limited spatial coherence of the vertical component, and may be interpreted as the smaller-scale active or universal motions. The nesting of smaller packets within larger ones, which are within even larger ones, and so on, creates the appearance of multiple zones of uniform streamwise momentum, which is an observed characteristic of the logarithmic layer (Meinhart & Adrian 1995).

The alignment of hairpin vortices in packets also explains several puzzling aspects of turbulent bursts. The classical bursting sequence, as observed by H_2 bubble visualization, is a wavering of the bubbles, followed by lift-up of the low-speed streak and a violent burst (Kline *et al.* 1967). However, in more modern work, Bogard & Tiederman (1986), Luchik & Tiederman (1987), and Tardu (1995) all conclude that the near-wall burst process consists of a sequence of Q2 events. In addition, Tardu (1995) shows that later events in a sequence become stronger, ultimately terminating in one exceptionally strong ejection. These fundamental aspects of turbulent bursts can also be explained by the passage of a streamwise arrangement of the hairpin vortices in a packet. The adjacency of hairpins within a packet clearly implies a sequence of Q2 events in space. It also results in strong internal shear layers caused by the induced downflow (Q4) from an upstream vortex head meeting the low-speed upflow (Q2) induced by an adjacent downstream vortex, cf. figure 11. This Q2/Q4 stagnation-point flow provides the source of the VITA signature, often used to identify burst processes. As a packet sweeps over the H_2 bubble wire, the passage of each hairpin would perturb the flow up and down (cf. figure 11 for an example of the oscillating streamlines in a packet), and the oscillation builds as the smaller end of the packet approaches, owing to the induction increasing as the scale of a hairpin decreases. At the end of the packet, the back-induced flow would be unopposed by the downwash of an upstream hairpin, and the bubbles would be ejected from the packet by the strongest hairpin, a combination that could produce a very strong upward motion.

Given the modern definition of a burst as a cluster of ejection events, it is highly likely that the turbulent burst process is a manifestation of the passage of a hairpin packet. The burst sequence is not a temporal oscillation, but merely a sequence of forced responses to the passage of the packet.

The preference for cane-shaped, one-sided hairpins observed by Guezennec *et al.* (1987) and Robinson (1991) has been explained by the fact that asymmetric hairpins autogenerate more rapidly than symmetric hairpins (Zhou *et al.* 1999). The packet created by a strongly asymmetric hairpin consists of an alternating sequence of right- and left-handed canes. If attention is confined to only the near-wall region ($y^+ < 60$), the behaviour of the packet is very similar to that proposed by Schoppa & Hussain (1997) and Jeong *et al.* (1997).

The mean growth angle of an inclined hairpin ramp $\gamma = 12^\circ$ is lower, on average, than the 20° angle found by Head & Bandyopadhyay (1981), but the latter is within the range of angles found in figure 24. The general trend for γ to increase with age/distance from the wall may explain some of the difference, since most of Head & Bandyopadhyay's observations were for the outer edge of the boundary layer, and our slope data is taken closer to the wall.

Brown & Thomas (1977) infer an 18° angle from the location of maximum correlation between the wall shear stress and u. This is also higher than present observations, but again, the correlation may tend to emphasize the outer flow. They interpreted their results in terms of the backs of turbulent bulges, which are essentially phenomena of the outermost edge of the boundary layer. Many other studies based on correlation or conditional averaging (cf. Chen & Blackwelder 1978; Alving, Smits & Watmuff 1990; MacAulay & Gartshore 1991, for example) have found angles ranging from 15° to 90°. It seems inevitable that without *a priori* knowledge of the general structure, statistical averaging methods will confound the various structures in the boundary layer – backs of bulges, hairpin inclinations and growth angles of hairpin packets. Many investigations interpret their results in terms of backs of bulges, which were

observable from visualization, but not in terms of internal hairpin packets, which must also have contributed to the average behaviour. Thus, the structural evidence is difficult to interpret. However, outer-scale structures such as backs and bulges and hairpin packets are related, especially in lower-Reynolds-number boundary layers where the hairpins extend to the top of the outer layer, and the bulges appear to be the sum of two or three hairpins. As the Reynolds number increases, Alving *et al.* (1990) observed that the bulges become less prominent, and the outer edge becomes flatter. This behaviour is likely to be associated with the number of hairpins in each packet increasing with Re_θ, since the amplitude of statistical fluctuations associated with a large collection of eddies will decrease as the number increases. MacAulay & Gartshore (1991) offer a similar interpretation.

The hairpin packet scenario clearly supports and gives specific interpretation to Townsend's (1976) attached eddy hypothesis which states that eddies attached to the wall grow in proportion to their distance from the wall in a self-similar fashion. Growing hairpins are consistent with this scenario, and the linear growth rate of the hairpins in a packet supports self-similarity, although it is understood that the young hairpins evolve through a non-similar series of shapes before becoming omega-shaped in their later stages. It is interesting that on a coarser scale, i.e. one that low-pass filters the cores of the hairpin vortices, the remaining flow pattern of a packet characteristically satisfies Townsend's attached eddy hypothesis.

Many aspects of the model described here can be found in the work of Perry and co-workers (Perry & Chong 1982; Perry, Henbest & Chong 1986; Marusic & Perry 1995; Perry & Marusic 1995) in which the boundary layer is conceived as a collection of randomly located hairpins whose properties are qualitatively compatible with those that have been found experimentally in this paper. The principal difference between the present observations and the lambda-vortex models of Perry and co-workers is the organization of hairpins into packets, and it is reasonable to ask how that difference might affect the quantitative behaviour of the flow. Following Zhou *et al.* (1997), let the velocity field of the αth hairpin at some instant be $\boldsymbol{u}_\alpha(\boldsymbol{x}, t)$, and let $\boldsymbol{u}(\boldsymbol{x}, t)$ be the total field

$$\boldsymbol{u}(\boldsymbol{x}, t) = \sum_\alpha \boldsymbol{u}_\alpha(\boldsymbol{x}, t). \tag{2}$$

For the purpose of illustrating the effect of grouping the hairpins, nonlinear interactions can be ignored. The mean Reynolds shear stress is

$$\overline{uv} = \overline{\sum_\alpha u_\alpha \sum_\beta v_\beta} = \sum_\alpha \overline{u_\alpha v_\alpha} + \sum_\alpha \sum_{\beta \neq \alpha} \overline{u_\alpha v_\beta}, \tag{3}$$

where the first term is the sum of Reynolds stresses from individual hairpins in the packet, and the second term is the contribution to the total Reynolds shear stress from the interaction of the hairpins. Essentially, it is the transport of u-momentum in the αth hairpin field by vertical motion of the field of the βth hairpin. The terms in this summation average to zero unless there is correlation between the spatial locations of the hairpins within a packet. Physically, this correlation enhances the Reynolds stress by the cooperative transfer of momentum between the hairpins, leading to a large-scale low-speed zone.

We call the last sum in (3) the coherent stress because it exists only when the hairpins are arranged coherently, and is thus absent in the random lambda-vortex models. The Reynolds stresses calculated in Perry & Marusic (1995) are based on such a model, and indeed differences exist between the model prediction and experiment. However,

addition to the model of a second group of structures, the physically detached 'type-B' eddies, leads to quite reasonable agreement. Prediction in either model might be improved by the addition of a coherent stress contribution. The magnitude of the coherent stress depends upon the spacing of the hairpins. Clearly, as the spacing grows beyond the support of the individual hairpins, the interaction diminishes and the coherent stress vanishes. Thus, organization of the hairpins within a packet is involved in creation of turbulent stresses, and modification of this organization may be an important method of manipulating wall turbulence.

The wide field of view data used in this research may currently be found following links on the web page of the Laboratory for Turbulence and Complex Flow at the Department of Theoretical and Applied Mechanics at the University of Illinois at Urbana-Champaign, *http://ltcf.tam.uiuc.edu*. Selected images of instantaneous vector fields are available for viewing and/or download, and all raw data is available for download.

This work was supported by grants from the Office of Naval Research and the National Science Foundation.

REFERENCES

Acarlar, M. S. & Smith, C. R. 1987*a* A study of hairpin vortices in a laminar boundary layer. Part 1. Hairpin vortices generated by a hemisphere protuberance. *J. Fluid Mech.* **175**, 1–41.

Acarlar, M. S. & Smith, C. R. 1987*b* A study of hairpin vortices in a laminar boundary layer. Part 2. Hairpin vortices generated by fluid injection. *J. Fluid Mech.* **175**, 43–83.

Adrian, R. J. 1991 Particle imaging techniques for experimental fluid mechanics. *Ann. Rev. Fluid Mech.* **23**, 261–304.

Adrian, R. J. 1996 Stochastic estimation of the structure of turbulent fields. In *Eddy Structure Identification* (ed. J. P. Bonnet), p. 145. Springer.

Adrian, R. J., Christensen, K. T. & Liu, Z.-C. 2000 On the analysis and interpretation of turbulent velocity fields. *Exps. Fluids* (accepted).

Adrian, R. J. & Moin, P. 1988 Stochastic estimation of organized turbulent structure: homogeneous shear flow. *J. Fluid Mech.* **190**, 531–559.

Adrian, R. J., Moin, P. & Moser, R. D. 1987 Stochastic estimation of conditional eddies in turbulent channel flow. *Proc. 1987 Summer Program, Report CTR-S87*, pp. 7–19. Center for Turbulence Research, Stanford University, Stanford, CA.

Alfredsson, P. H. & Johansson, A. V. 1984 Time scales in turbulent channel flow. *Phys. Fluids* **27**, 1974–1981.

Alving, A. E., Smits, A. J. & Watmuff, J. H. 1990 Turbulent boundary layer relaxation from convex curvature. *J. Fluid Mech.* **211**, 529–556.

Balint, J.-L, Wallace, J. M. & Vukoslavcevic, P. 1991 The velocity and vorticity vector fields of a turbulent boundary layer. Part 2. Statistical properties. *J. Fluid Mech.* **228**, 53–86.

Bandyopadhyay, P. R. 1980 Large structure with a characteristic upstream interface in turbulent boundary layers. *Phys. Fluids* **23**, 2326–2327.

Bandyopadhyay, P. R. 1983 Turbulent spot-like feature of a boundary layer. *Ann. NY Acad. Sci.* **404**, 393–395.

Blackwelder, R. F. & Haritonidis, J. H. 1983 The bursting frequency in turbulent boundary layers. *J. Fluid Mech.* **132**, 87–103.

Blackwelder, R. F. & Kaplan, R. E. 1976 On the wall structure of the turbulent boundary layer. *J. Fluid Mech.* **76**, 89–112.

Bogard, D. G. & Tiederman, W. G. 1986 Burst detection with single-point velocity measurements. *J. Fluid Mech.* **162**, 389–413.

Brooke, J. W. & Hanratty, T. J. 1993 Origin of turbulence-producing eddies in a channel flow. *Phys. Fluids* A **5**, 1011–1022.

Brown, G. R. & Thomas, A. S. W. 1977 Large structure in a turbulent boundary layer. *Phys. Fluids* **20**, S243–251.

Chacin, J. M., Cantwell, B. J. & Kline, S. J. 1996 Study of turbulent boundary layer structure using the invariants of the velocity gradient tensor. *Exps. Therm. Fluid Sci.* **13**, 308–317.

Chen, C. H. P. & Blackwelder, R. F. 1978 Large scale motion in a turbulent boundary layer: a study using temperature signals in bounded shear flows. *J. Fluid Mech.* **83**, 209–224.

Chong, M. S., Perry, A. E. & Cantwell, B. J. 1990 A general classification of three-dimensional flow fields. *Phys. Fluids* A **2**, 765–777.

Chong, M. S., Soria, J., Perry, A. E., Chacin, J., Cantwell, J. & Na, Y. 1998 Turbulence structures of wall-bounded shear flows found using DNS data. *J. Fluid Mech.* **357**, 225–247.

Clauser, F. 1956 The turbulent boundary layer. *Adv. Appl. Mech.* **4**, 1–51.

Coles, D. E. 1962 The turbulent boundary layer in a compressible fluid. *RAND Corp. Rep. R-403-PR*.

Falco, R. E. 1977 Coherent motions in the outer region of turbulent boundary layers. *Phys. Fluids* **20**, 124–132.

Falco, R. E. 1991 A coherent structure model of the turbulent boundary layer and its ability to predict Reynolds number dependence. *Phil. Trans. R. Soc. Lond.* **336**, 103–129.

Grant, H. L. 1958 The large eddies of turbulent motion. *J. Fluid Mech.* **4**, 149.

Guezennec, Y. G., Piomelli, U. & Kim, J. 1987 Conditionally-averaged structure in wall-bounded turbulent flow. *Proc. 1987 Summer Program, Report CTR-S87*, pp. 263–272. Center for Turbulence Research, Stanford University, Stanford, CA.

Haidari, A. H. & Smith, C. R. 1994 The generation and regeneration of single hairpin vortices. *J. Fluid Mech.* **277**, 135–162.

Head, M. R. & Bandyopadhyay, P. 1981 New aspects of turbulent boundary-layer structure. *J. Fluid Mech.* **107**, 297–338.

Jeong, J. & Hussain, F. 1995 On the identification of a vortex. *J. Fluid Mech.* **285**, 69–94.

Jeong, J., Hussain, F., Schoppa, W. & Kim, J. 1997 Coherent structure near the wall in a turbulent channel flow. *J. Fluid Mech.* **332**, 185–214.

Kim, J. 1987 Evolution of a vortical structure associated with the bursting event in a channel flow. In *Turbulent Shear Flows 5* (ed. F. Durst, B. E. Launder, J. L. Lumley, F. W. Schmidt & J. H. Whitelaw), pp. 221–233. Springer.

Kim, J., Moin, P. & Moser, R. D. 1987 Turbulent statistics in fully developed channel flow at low Reynolds number. *J. Fluid Mech.* **177**, 133–166.

Kim, J. & Spalart, P. R. 1987 Scaling of the bursting frequency in turbulent boundary layers at low Reynolds number. *Phys. Fluids* **30**, 3326–3328.

Klewicki, J. C. 1989 On the interactions between the inner and outer region motions in turbulent boundary layers. PhD dissertation, Michigan State University, East Lansing, Michigan, USA.

Klewicki, J. C. & Falco, R. E. 1990 On accurately measuring statistics associated with small-scale structure in turbulent boundary layers using hot-wire probes. *J. Fluid Mech.* **219**, 119–142.

Kline, S. J., Reynolds, W. C., Schraub, F. A. & Runstadler, P. W. 1967 The structure of turbulent boundary layers. *J. Fluid Mech.* **30**, 741–773.

Kline, S. J. & Robinson, S. K. 1989 Quasi-coherent structures in the turbulent boundary layer. Part I: status report on a community-wide summary of the data. In *Near Wall Turbulence* (ed. S. J. Kline & N. H. Afgan), pp. 218–247. Hemisphere.

Kovasznay, L. S. G., Kibens, V. & Blackwelder, R. F. 1970 Large scale motion in the intermittant region of a turbulent boundary layer. *J. Fluid Mech.* **41**, 283–325.

Liu, Z. C. & Adrian, R. J. 1998 Visualization of hairpin vortex structure with PIV and DNS. 8th Intl Symp. on Flow Visualization, Sorrento, Italy, 1–4 September 1998.

Liu, Z. C., Adrian, R. J. & Hanratty, T. J. 1991 High resolution measurement of turbulent structure in a channel with particle image velocimetry. *Exps. Fluids* **10**, 301–312.

Luchik, T. S. & Tiederman, W. G. 1987 Time-scale and structure of ejections and bursts in turbulent channel flows. *J. Fluid Mech.* **174**, 529–552.

MacAulay, P. & Gartshore, I. P. 1991 A tentative model of outer layer structure in a turbulent boundary-layer developing on a smooth wall. In *Experimental Heat Transfer, Fluid Mechanics, and Thermodynamics* (ed. J. F. Keffer, R. K. Shah & E. N. Ganic). Elsevier.

Marusic, I. & Perry, A. E. 1995 A wall-wake model for the turbulence structure of boundary layers. Part 2. Further experimental support. *J. Fluid Mech.* **298**, 389–407.

MEINHART, C. D. 1994 Investigation of turbulent boundary-layer structure using particle-image velocimetry. PhD dissertation, University of Illinois, Urbana, Illinois, USA.

MEINHART, C. D. & ADRIAN, R. J. 1995 On the existence of uniform momentum zones in a turbulent boundary layer. *Phys. Fluids* **7**, 694–696.

MEINHART, C. D., PRASAD, A. K. & ADRIAN, R. J. 1993 A parallel digital processor for particle image velocimetry. *Meas. Sci. Technol.* **4**, 619–626.

NAGUIB, A. M. & WARK, C. E. 1992 An investigation of wall-layer dynamics using a combined temporal filtering and correlation technique. *J. Fluid Mech.* **243**, 541–560.

NYCHAS, S. G., HERSHEY, H. C. & BRODKEY, R. S. 1973 A visual study of turbulent shear flow. *J. Fluid Mech.* **61**, 513–540.

PERRY, A. E. & CHONG, M. S. 1982 On the mechanism of wall turbulence. *J. Fluid Mech.* **119**, 173–217.

PERRY, A. E., HENBEST, S. & CHONG, M. S. 1986 A theoretical and experimental study of wall turbulence. *J. Fluid Mech.* **165**, 163–199.

PERRY, A. E. & MARUSIC, I. 1995 A wall-wake model for the turbulence structure of boundary layers. Part 1. Extension of the attached eddy hypothesis. *J. Fluid Mech.* **298**, 361–388.

PRASAD, A. K., ADRIAN, R. J., LANDRETH, C. C. & OFFUTT, P. W. 1992 Effect of resolution on the speed and accuracy of particle image velocimetry interrogation. *Exps. Fluids* **13**, 105–116.

PRATURI, A. K. & BRODKEY, R. S. 1978 A stereoscopic visual study of coherent structures in turbulent shear flow. *J. Fluid Mech.* **89**, 251–272.

ROBINSON, S. K. 1991 Coherent motion in the turbulent boundary layer. *Ann. Rev. Fluid Mech.* **23**, 601–639.

ROBINSON, S. K. 1993 The kinematics of turbulent boundary layer structure. *NASA Tech. Mem.* 103859.

ROGERS, M. M. & MOIN, P. 1987 The structure of the vorticity field in homogeneous turbulent flows. *J. Fluid Mech.* **176**, 33–66.

SCHOPPA, W. & HUSSAIN, F. 1997 Genesis and dynamics of coherent structures in near-wall turbulence: a new look. In *Self-Sustaining Mechanisms of Wall Turbulence* (ed. R. L. Panton), pp. 385–422. Computational Mechanics, Southampton, UK.

SINGER, B. A. & JOSLIN, R. D. 1994 Metamorphasis of a hairpin vortex into a young turbulent spot. *Phys. Fluids* **6**, 3724–3736.

SIROVICH, L. 1997 Dynamics of coherent structures in wall bounded turbulence. In *Self-Sustaining Mechanisms of Wall Turbulence* (ed. R. L. Panton), pp. 333–364, Computational Mechanics, Southampton, UK.

SMITH, C. R. 1984 A synthesized model of the near-wall behavior in turbulent boundary layers. In *Proc. 8th Symp. on Turbulence* (ed. J. Zakin & G. Patterson), pp. 299–325, University of Missouri-Rolla.

SMITH, C. R., WALKER, J. D. A., HAIDARI, A. H. & SOBRUN, U. 1991 On the dynamics of near-wall turbulence. *Phil. Trans. R. Soc. Lond.* A **336**, 131–175.

SPALART, P. R. 1988 Direct simulation of a turbulent boundary layer up to $Re_\theta = 1410$. *J. Fluid Mech.* **187**, 61–98.

SPALDING, D. B. 1961 A single formula for the law of the wall. *Trans. ASME* C: *J. Appl. Mech.* **28**, 455–458.

TARDU, S. 1995 Characteristics of single and clusters of bursting events in the inner layer, Part 1: Vita events. *Exps Fluids* **20**, 112–124.

THEODORSEN, T. 1952 Mechanism of turbulence. In *Proc. 2nd Midwestern Conf. on Fluid Mech.*, pp. 1–19, Ohio State University, Columbus, Ohio.

TOMKINS, C. D. 1997 A particle image velocimetry study of coherent structures in a turbulent boundary layer. MS thesis, University of Illinois, Urbana, Illinois, USA.

TOWNSEND, A. A. 1958 The turbulent boundary layer. In *Boundary Layer Research* (ed. H. Görtler), p. 1. Springer.

TOWNSEND, A. A. 1976 *The Structure of Turbulent Shear Flow*, 2nd edn. Cambridge University Press.

WALEFFE, F. & KIM, J. 1997 How streamwise rolls and streaks self-sustain in a shear flow. In *Self-Sustaining Mechanisms of Wall Turbulence* (ed. R. L. Panton), pp. 309–332. Computational Mechanics, Southampton, UK.

WALLACE, J. M., BRODKEY, R. S. & ECKELMANN, H. 1977 Pattern-recognized structures in bounded turbulent shear flows. *J. Fluid Mech.* **83**, 673–693.

WARK, C. E. & NAGIB, H. M. 1988 Scaling of frequency of Reynolds-stress producing events in regular and manipulated boundary layers. In *Proc. Zoran Zaric Memorial Seminar on Near-Wall Turbulence*. Dubrovnik, Yugoslavia.

WARK, C. E. & NAGIB, H. M. 1989 Relation between outer structures and wall-layer events in boundary layers with and without manipulation. In *Structure of Turbulence and Drag Reduction* (ed. A. Gyr), pp. 467–474. Springer.

WESTERWEEL, J. 1994 Efficient detection of spurious vector in particle image velocimetry data. *Exps. Fluids* **16**, 236–247.

ZHOU, J., ADRIAN, R. J. & BALACHANDAR, S. 1996 Autogeneration of near-wall vortical structures in channel flow. *Phys. Fluids* **8**, 288–290.

ZHOU, J., ADRIAN, R. J., BALACHANDAR, S. & KENDALL, T. M. 1999 Mechanisms for generating coherent packets of hairpin vortices in channel flow. *J. Fluid Mech.* **387**, 353–396.

ZHOU, J., MEINHART, C. D., BALACHANDAR, S. & ADRIAN, R. J. 1997 Formation of coherent hairpin packets in wall turbulence. In *Self-Sustaining Mechanisms of Wall Turbulence* (ed. R. L. Panton), pp. 109–134. Computational Mechanics, Southampton, UK.